CHALMERS

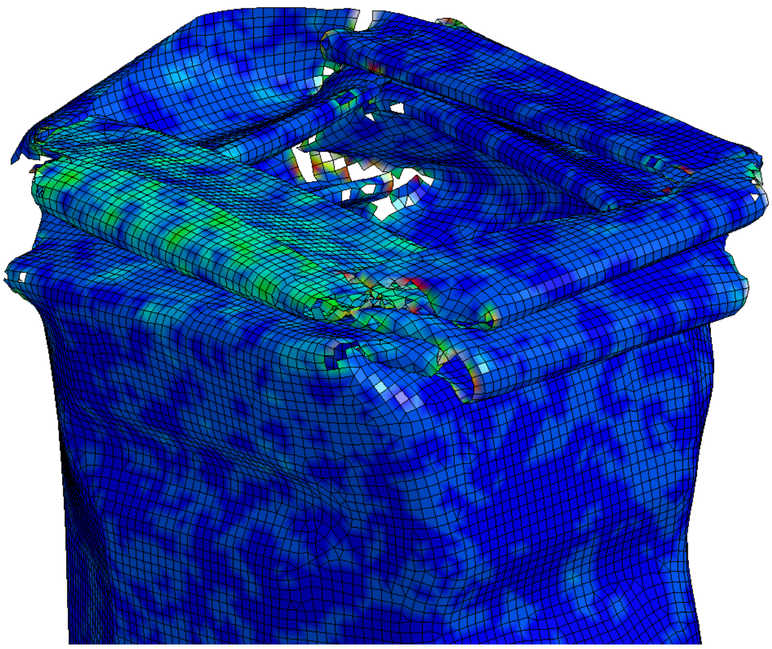

Evaluation of strain path independent material models for failure prediction in sheet metals using LS-DYNA

Master's thesis in Material Mechanics

STEFAN ASK
ANDERS SELLGREN

Department of Applied Mechanics
CHALMERS UNIVERSITY OF TECHNOLOGY
Göteborg, Sweden 2016

MASTER'S THESIS IN MATERIAL MECHANICS

Evaluation of strain path independent material models for failure prediction in sheet metals using LS-DYNA

STEFAN ASK
ANDERS SELLGREN

Department of Applied Mechanics
Division of Material & Computational Mechanics
CHALMERS UNIVERSITY OF TECHNOLOGY

Göteborg, Sweden 2016

Evaluation of strain path independent material models for failure prediction in sheet metals using LS-DYNA
STEFAN ASK
ANDERS SELLGREN

Master's thesis 2016:33
ISSN 1652-8557
Department of Applied Mechanics
Division of Material & Computational Mechanics
Chalmers University of Technology
SE-412 96 Göteborg
Sweden
Telephone: +46 (0)31-772 1000

Cover:
An UHS boron steel crash box, deformed by a $75\,kg$ rigid plate dropped from a height of $5.10\,m$. The first principal strain rate suggested by the VCC-model is fringe plotted.

Chalmers Reproservice
Göteborg, Sweden 2016

Evaluation of strain path independent material models for failure prediction in sheet metals using LS-DYNA
Master's thesis in Material Mechanics
STEFAN ASK
ANDERS SELLGREN
Department of Applied Mechanics
Division of Material & Computational Mechanics
Chalmers University of Technology

Abstract

At Volvo Cars, CrachFEM in combination with LS-DYNA, is currently used for failure prediction in car crash simulations. CrachFEM is a computationally costly algorithm, and for that reason Volvo Cars is looking for an alternative to this model. A new model, here called the VCC-model, has been developed at Volvo Cars with the intention to be used in full scale car crash simulations.

The objective of this Master's thesis is to investigate whether or not the VCC-model have the potential of being a suitable alternative to CrachFEM in car crash simulations.

CrachFEM is compared with two different implementations of the VCC-model, here referred to as DIEM and the VCC-model. All models are developed with the purpose to be able to handle the problem of non-linear strain paths. Hence, the problems chosen in the current study do all exhibit non-linear or broken strain paths. The three models are analyzed and evaluated in applications ranging from simple single element models up to full scale car models.

Some unexplainable differences in results obtained with DIEM and the VCC-model were observed. It turns out that CrachFEM yields dramatically different failure predictions in some of the analyzed load cases. These differences have to be investigated further through physical experiments.

Keywords: Failure, Necking, Fracture, Sheet metal, Strain path independency

Preface

This thesis is written as a completion of the Master's programme Applied Mechanics at Chalmers University of Technology. The work has been carried out at DYNAmore Nordic AB, in Gothenburg. The supervisors for the project have been Dr. Per-Anders Eggertsen at Volvo Cars, Dr. Kjell Mattiasson at Chalmers University of Technology, and MSc Torbjörn Johansen at DYNAmore Nordic AB. The examiner of the project has been Dr. Kjell Mattiasson.

First of all we would like to thank Dr. Johan Jergéus at Volvo Cars for initiating the project and for creating the best possible conditions for us to succeed.

We would like to express our appreciation to Torbjörn Johansen for sharing his expertise in LS-DYNA, and for always being willing to support us. We would also like to show our gratitude towards the other employees at DYNAmore Nordic AB for taking the time helping us, and for providing a friendly environment.

A special thanks to Per-Anders Eggertsen and Kjell Mattiasson for sharing their specialist knowledge, enabling us to complete this Master's thesis. They have also provided an extensive guidance throughout the entire project, for which we are very grateful.

Stefan Ask & Anders Sellgren
Gothenburg, June 2016

Contents

1 Introduction

During last year (December 2014-November 2015) 267 people were killed in traffic related accidents on the Swedish roads. This is a decrease by 5% from the calculated mean from the previous four years, still it is approximately five people a week getting killed in traffic [1].

It is obvious that vehicle safety is a very important area in the automotive industry. Maybe the most important safety aspect of all is how a car body performs and deforms during a crash event.

Real life controlled car crashes are expensive to execute, which is why the automotive industry relies heavily on computer simulations these days.

1.1 Background

The material response has a major influence on the car in impact situations. Hence, the accuracy of the material modeling is crucial for the reliability of the simulation results.

At Volvo Cars a commercial program called CrachFEM, developed by MATFEM, is used for material modeling and failure prediction of sheet metal parts. This program is used together with the explicit FE-code LS-DYNA. CrachFEM was developed to be able to handle nonlinear and broken strain paths in sheet metal forming simulations. However it has been shown that CrachFEM behaves questionable for certain strain paths [2]. Another thing to note is that CrachFEM is a very time consuming algorithm, a fact that has motivated Volvo Cars to investigate alternatives to this model.

At Volvo Cars an alternative approach for failure prediction in sheet metal has been implemented as a user-defined (UMAT, user material subroutine) material model with coupled failure criterion in LS-DYNA. This material model will be referred to as the VCC-model.

In addition, the failure criterion of the VCC-model has been implemented, by Thomas Borrvall at Dynamore Nordic AB, as a part of DIEM under the keyword *MAT_ADD_EROSION in LS-DYNA. This keyword can be used as an addition to different material models to indicate failure and erode elements during simulations.

A comprehensive comparison between the two implementations of the VCC-model, presented above, has not yet been carried out.

1.2 Objectives

The purpose of the current work is to evaluate whether or not the VCC-model has the potential of being a suitable alternative to CrachFEM in simulations with nonlinear and broken strain paths. In the numerical studies performed within the current study three different models and/or implementations are compared. These are CrachFEM, the implementation of the VCC-model as a user subroutine and, finally, the VCC-model implemented in DIEM.

Initially the three models will be compared by subjecting one single finite element to various broken strain paths, from different states of pre-strain, and noting at what strain level and in what mode the three different models indicates failure. This is done in order to get an idea of in what situations the different models conform and in what situations they deviate.

There are different ways of predicting plastic instability in sheet metals. The conventional way is to use a so called forming limit curve (FLC). Another way of predicting instability is a finite element based Marciniak–Kuczynski (M-K) approach where no failure curves are used, but rather the material's hardening curve and the shape of the yield surface determines the limit of plastic instability. The VCC-model is based on the assumption that the material hardens in a purely isotropic manner. However most metals undergoes mixed isotropic-kinematic hardening during plastic deformation. In this context the FE-based M-K approach will be used to get an indication of the effects kinematic hardening has on the instability prediction.

The intention with the VCC-model is that it will be used in full scale car crash simulations, which is a highly complex load case. Another rather complex, more comprehensible load case, is the axial compression of a crash box. Hence, to compare and evaluate the models in a more challenging deformation scenario crash box simulations will be performed.

Simulation time is expensive, and is, thus, an important aspect of all simulations. For that reason a study of the simulation time used by the models will be done in a full scale car crash simulation.

A brief summary of the goals of this Master's thesis are.

1. Evaluate the behaviour of the presented models on one finite element.
2. Analyze the models in the complex loading scenario of a crash box simulation.
3. Examine the simulation time of the models in a full scale car crash event.
4. Investigate a FE-based M-K approach with respect to mixed isotropic-kinematic hardening.

1.3 Limitations

1. Only the above presented models will be compared and investigated during the work.
2. The work will only consider hot-formed boron steel.
3. No material strain rate dependence will be considered in the project.

2 Fundamentals of car crash physics and material behaviour

2.1 Car crash physics

The trend in the car industry nowadays is to manufacture lighter cars using materials with an increased strength to weight ratio. However, these types of materials are often brittle and from a crashworthiness point of view this causes problems in impact situations where ductile materials are preferred [3]. Ductile materials are capable of dissipating energy during a longer period of time at a lower mean crushing force, and low crushing forces saves lives in impact situations.

Newton's second law of motion states that impulse equals change in momentum. Impulse is also the time integral of the applied force

$$I = \Delta p = m \cdot \Delta v = \int_{t_1}^{t_2} F dt \tag{2.1}$$

Looking at Eq 2.1 it is evident that stopping a car, with mass m, driving at a certain velocity requires a certain impulse. This impulse can be achieved by either stopping the car rapidly or during a long period of time, the former requires a large force and the latter a smaller force. To generate a modest deceleration of the car, and hopefully save its occupants, a small force during a long time is preferred to stop the vehicle. This is where the crash box comes into play; it ensures that the vehicle decelerates during a long period of time, at a low mean force.

2.1.1 The role of crash boxes

A crash box is a thin-walled box-beam that is designed with strategically placed geometrical discontinuities, called triggers, in order to deform in a very specific, controlled and repeatable manner during axial loading. Repeatable in the sense that all crash boxes of the same type manufactured should deform in the same way.

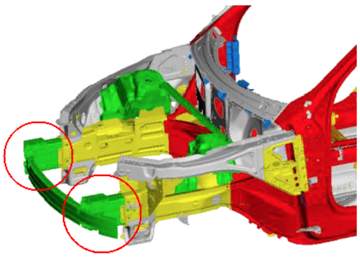

Figure 2.1: *The crash boxes in the new Volvo XC 90 car, marked with red circles, are made of aluminium.*

There are generally two crash boxes in the front part of a passenger car, that make up the vehicle's crumple zone. The crash boxes are responsible for the majority of the kinetic energy absorption, in a frontal collision event, by plastic deformations. The vehicle's kinetic energy is converted into heat and sound during the plastic collapse of the crash boxes. The remainder of the kinetic energy is absorbed through plastic deformation of other parts of the car, such as the hood and the front fenders.

The energy absorbed by the axial compression of a crash box can be expressed as the area under the force-displacement curve

$$E_A = \int_0^\delta F(x)dx \tag{2.2}$$

where δ is the axial compression length and $F(x)$ is the crushing force. This equation imposes a dilemma; since low deceleration forces are of vital importance, long crash boxes would be required to get a large integral in Eq 2.2. However, long crumple zones creates contradictions with the exterior design department. Thus, clever solutions has been devised in order to manufacture compact crash boxes with capabilities of large energy absorption.

A key parameter when discussing a deformable body's ability to absorb energy is its Specific Energy Absorption, abbreviated SEA. It is a measure of the energy consumption per unit mass of the deformed component

$$SEA = \frac{E_A}{m} \tag{2.3}$$

The ideal crash box should have a high SEA value, i.e. it should be light-weight and be able the absorb a considerable amount of energy during a stable ductile axial plastic collapse. From an aesthetic point of view it should also be short and compact. Hence, designing crash boxes is a balancing act between crashworthiness and aesthetics.

2.2 Properties of boron steel and its use

The material studied in the current work is an ultra high-strength (UHS) hot-formed martensitic boron steel, which has a relatively low ductility. The use of boron steel has increased strongly in recent years and today the body-in-white (BIW) of the new Volvo XC 90 car consists of 33 weight % of various types of boron steels. It is distributed around the cab, to form a stiff cage around the driver and passengers, according to Figure 2.2.

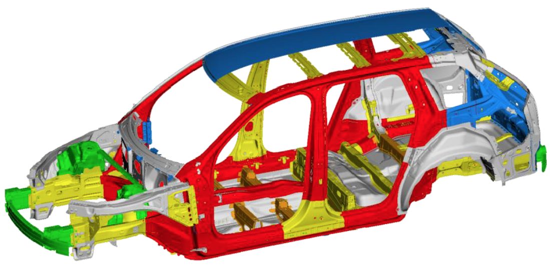

Figure 2.2: *The body-in-white of the new Volvo XC 90 car. The red parts are made of boron steel [4].*

This work focuses on one type of these boron steels, with the material properties presented in Table 2.1.

Young's modulus, E	Poisson's ratio, ν	Yield stress, σ_Y	Density, ρ
204 [GPa]	0.3 [-]	1143 [MPa]	7800 [kg/m^3]

Table 2.1: Material properties of the boron steel used in the current work.

The forming limit curve and the hardening curve of the boron steel are shown in Figure 2.3.

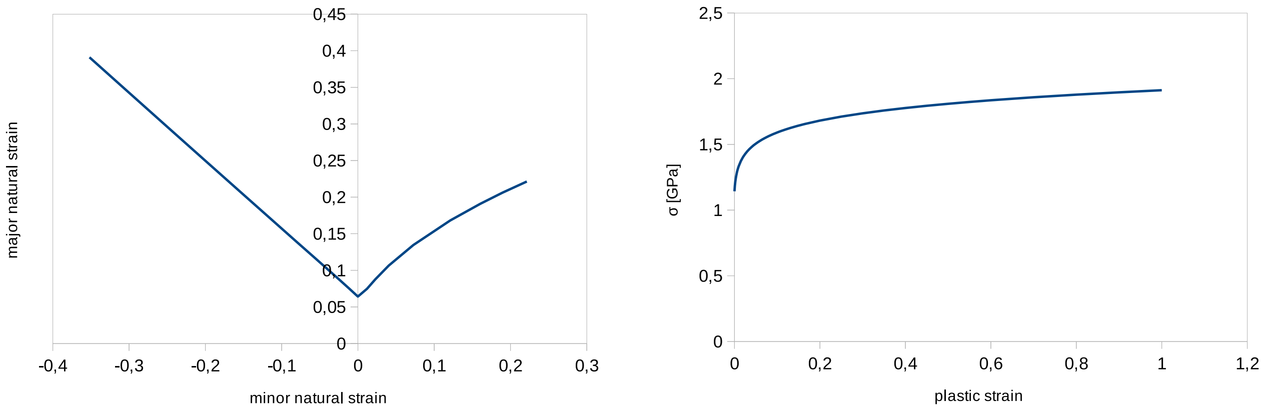

(a) *The forming limit curve (FLC).* (b) *The hardening curve.*

Figure 2.3: *The FLC and the hardening curve of the studied boron steel.*

2.3 Hardening models

In purely isotropic hardening the yield surface remains the same shape but expands uniformly with the evolution of plastic strain. This type of hardening is illustrated in Figure 2.4a. The magnitude of the expansion is defined by the drag-stress κ,

Under subsequent reverse loading most metals undergoes early re-yielding, usually referred to as the Baushinger effect. On a material modeling level this is accounted for by introducing some kind of kinematic hardening model. This type of hardening is used to model properties of materials exhibited when subjected to rapid changes of strain paths, mainly where the strain paths switches sign. In a pure kinematic hardening model, the yield surface remains the same size and shape but translates with the back-stress $\boldsymbol{\alpha}$, as is illustrated in Figure 2.4b. In a similar fashion as for isotropic hardening this effect depends on the evolution of the plastic strain.

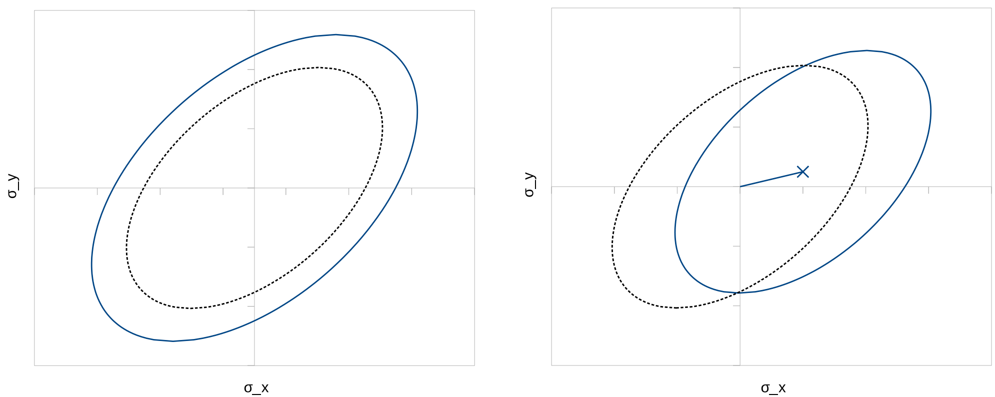

(a) *Isotropic hardening* (b) *Kinematic hardening*

Figure 2.4: *Purely isotropic and purely kinematic hardening represented in stress space.*

However, metals often undergoes both isotropic and kinematic hardening during plastic deformation. This type of hardening can, for instance, be modeled by mixed kinematic-isotopic hardening with the following yield function

$$\Phi = \sigma_e^{red} - \sigma_y - \kappa \quad \text{where} \quad \sigma_e^{red} = \sqrt{\frac{3}{2}}|\boldsymbol{\sigma}_{dev}^{red}| \quad \text{with} \quad \boldsymbol{\sigma}_{dev}^{red} \stackrel{\text{def}}{=} \boldsymbol{\sigma}_{dev} - \boldsymbol{\alpha}_{dev} \tag{2.4}$$

where $\Phi = 0$ defines the yield surface in stress space [5]. The initial yield surface is given by σ_y and the hardening stresses are defined as

$$\kappa = -\beta H k \quad \text{and} \quad \boldsymbol{\alpha}_{dev} = -\frac{2}{3}[1 - \beta] H \boldsymbol{a}_{dev} \tag{2.5}$$

The proportion of kinematic and isotropic hardening in the mixed hardening case is in this work described by the hardening parameter $\beta \in [0, 1]$.

3 Failure mechanisms in metal sheets

Damage, failure and fracture are three words that are commonly used in the context of material modelling. The difference between these terms is something that not everyone is clear on, it may even be a subject that is confusing to the reader.

Damage is here referred to as physical discontinuities in the material, such as micro-voids, which are often induced during the manufacturing process. The definition of failure adopted in the current work is; the inability of the material to meet certain criteria. Which can mean either of the two phenomena; plastic instability (necking) or fracture.

3.1 Plastic instability

When subjecting sheet metals to uniaxial tensile loadings the deformation field is uniform up to a specific point. If the load is increased further the uniformity of the deformation field is lost and a neck, over the width of the sheet, is formed. This is known as diffuse necking, and it coincides chronologically with the applied force maximum.

In a uniaxial tensile test the diffuse instability limit is well defined. Equilibrium states that the internal stress has to balance the applied force P

$$P = \sigma A \tag{3.1}$$

From experiments it is known that the force has a maximum at the diffuse limit, hence

$$dP = d\sigma \cdot A + \sigma \cdot dA = 0 \Rightarrow \frac{d\sigma}{\sigma} = -\frac{dA}{A} \tag{3.2}$$

To fulfill plastic incompressibility the following has to hold

$$dl \cdot A + L \cdot dA = 0 \Rightarrow \frac{dl}{L} = -\frac{dA}{A} = d\epsilon \tag{3.3}$$

Which results in

$$\frac{d\sigma}{d\epsilon} = \sigma \tag{3.4}$$

This means that diffuse instability occurs when the slope of the hardening curve is equal to the stress, i.e. the diffuse instability limit depends exclusively on the material hardening and the yield function. The formation of a diffuse neck is well defined and only observable in the uniaxial tensile test. Nevertheless, there is a similar phenomenon in the case of bi-axial straining where the deformation field loses its homogeneity. However, there is no universal definition of the diffuse limit in this case.

Localized necking is a phenomena that occurs after the diffuse instability limit. It is characterized by a drastic redistribution of strains in the sheet. The strains will eventually localize and form a narrow strip across the sheet in which there is a pronounced reduction of thickness (Figure 3.1). When the localized neck starts developing the stress field in the neck is no longer plane, but rather a three-dimensional stress state.

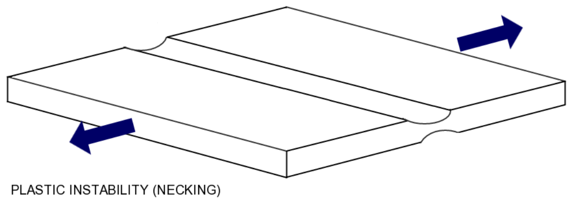

Figure 3.1: *A local neck in a sheet metal.*

The rapid increase in strain rate in the neck region is followed by damage growth, after which the material eventually fails in either ductile normal fracture (DNF) or ductile shear fracture (DSF). Normally fracture occurs very soon after the formation of the localized neck. This is due to the fact that all in-plane displacements are translated into a thickness reduction in a very limited part of the sheet. This increases the strain rate considerably and fracture is eventually unavoidable.

3.2 Fracture modes

There are two types of fractures; brittle and ductile fracture. A brittle fracture is preceded by an insignificant plastic deformation, e.g. the fracture of glass and ceramics. Prior to a ductile fracture there is, on the other hand, an excessive plastic deformation, e.g. the fracture of lead.

Sheet metals can break in two different modes, either in DNF or DSF. Ductile normal fracture is caused by the supervention of micro-voids, which subsequently grow and merge with each other to finally end in a ductile fracture.

Ductile shear fracture, on the other hand, is the result of shear band localization, which may be caused by previously formed micro-voids. These shear bands can form either through the thickness or in the plane of the metal sheet.

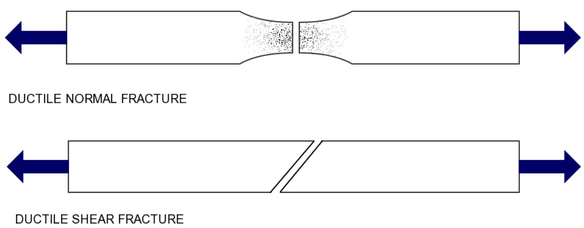

Figure 3.2: *The two possible fracture modes that can occur in sheet metals.*

In what mode the sheet fractures, depends highly on the stress state in the material and of the material composition.

3.2.1 Failure evolution

There are three different failure evolution scenarios that can occur in sheet metals according to Figure 3.3. In the first case damage growth is preceded by the formation of a neck, which means that the final fracture is a direct result of the strain concentrations in the neck.

In the second case the localized necking is preceded by damage growth. The high strain rate in the neck subsequently accelerates the damage growth. This finally ends with the material fracturing in either DNF or DSF.

In the third case no neck is formed. Instead damage starts to grow at a specific point and the final fracture becomes a consequence of micro-void growth and coalescence.

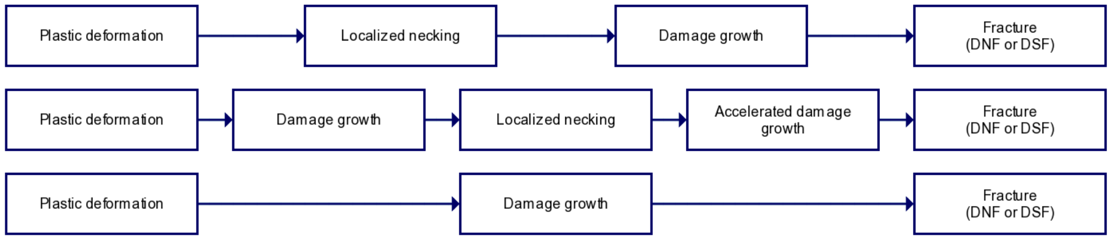

Figure 3.3: *Three possible scenarios of failure evolution in sheet metals [2]*

.

Experience has shown that case one, where the damage growth is preceded by the formation of a neck, is undoubtedly the most common failure scenario [2].

4 Methods for necking prediction

4.1 The forming limit diagram (FLD)

The forming limit diagram is a more than 50 years old concept, and it originates from the forming industry. The axes in the FLD are the major and minor strains, which are the largest and smallest in-plane principal strains, respectively [6]. The major strain, ϵ_1, is represented on the vertical axis and the minor strain, ϵ_2, on the horizontal axis.

The FLD consists of a forming limit curve (FLC), that is normally constructed by experimentally subjecting steel sheets to linear strain paths up to necking. Hence, the FLC is the limit where a localized neck starts developing. Plane strain is the most crucial strain path, whereas equi-biaxaial strain and pure shear results in much higher necking strains.

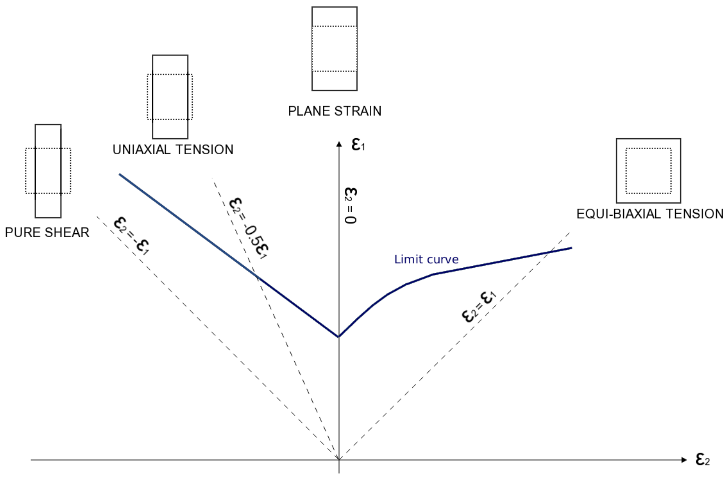

Figure 4.1: *A forming limit diagram (FLD) with an associated forming limit curve (FLC).*

A strain path in the FLD is defined by ρ, which is the ratio between the minor and major in-plane principal strain rates, i.e. $\rho = \dot{\epsilon}_2/\dot{\epsilon}_1$. Defining ρ like this makes it possible to describe non-linear and broken strain paths, as well as linear ones. For piecewise linear (broken) strain paths ρ_i defines the i:th linear part. For isotropic material in the case of uniaxial tension $\rho = -0.5$, as can be seen in Figure 4.1.

4.2 The forming limit represented in other variable spaces

It should be stressed that a FLC is constructed with linear strain paths up to necking. Unfortunately, the necking strains are strongly strain path dependent. This is a major problem in car crash situations where broken strain paths are common.

However, it can be shown that under the assumption of isotropic hardening a necking limit curve expressed in principal stress space is path independent [2]. Such a curve is called a forming limit stress curve (FLSC) and is situated in a forming limit stress diagram (FLSD). The FLSC can be constructed by a variable transformation from the principal strain space to the principal stress space. This path independency can be shown to also prevail in other specific variable spaces as well. Such a variable space is the $\alpha - \bar{\epsilon}^p$ space, in which the limit curve is expressed in terms of the effective plastic strain, $\bar{\epsilon}^p$, and the principal plastic strain rate ratio, $\alpha = \dot{\epsilon_2}^p/\dot{\epsilon_1}^p$.

Damage growth is strongly coupled to the stress triaxility η, defined as the ratio between mean stress and the von Mises stress. For that reason this variable space is commonly used in models describing fracture failure.

A limit curve in the $\eta - \bar{\epsilon}^p$ space is also strain path independent, and is hence often used for necking and fracture limit curves.

4.2.1 The $\alpha - \bar{\epsilon}^p$ variable space

The FLSD has never gained popularity among practicing engineers, probably because it is more straightforward thinking in terms of strains than in terms of stresses. The use of a limit curve in the $\alpha - \bar{\epsilon}^p$ space has, thus, greater possibilities of being accepted by people in the industry[2].

Knowing the material's hardening curve and the yield condition, the FLC in the principal strain space can be transformed to the $\alpha - \bar{\epsilon}^p$ space. In this variable space it is easy to realize what it means to choose a pre-strain that results in an effective plastic strain that is under or above the effective plastic strain corresponding to plastic instability in plane strain.

Principal plastic strain rate ratio α

The direction of plastic strain rate can be expressed in terms of the gradient of the plastic potential, f

$$\dot{\boldsymbol{\epsilon}}^p = \lambda \frac{\partial f}{\partial \boldsymbol{\sigma}} \tag{4.1}$$

where λ is the the plastic multiplier [5]. If the plastic potential, also known as the flow function, is chosen the to be the same as the yield function the flow rule of Eq 4.1 is said to be associative, this is oftentimes referred to as the *normality rule*. From the definition of effective plastic strain rate it can easily be shown that the plastic multiplier is equal to the effective plastic strain rate [7]. Hence, the associative flow rule can be written

$$\dot{\boldsymbol{\epsilon}}^p = \dot{\bar{\epsilon}}^p \frac{\partial \bar{\sigma}}{\partial \boldsymbol{\sigma}} \tag{4.2}$$

Assuming plane stress and the von Mises yield function, the effective stress can be defined in terms of the in-plane principal stresses

$$\bar{\sigma} = \sqrt{\sigma_1^2 - \sigma_1 \sigma_2 + \sigma_2^2} \tag{4.3}$$

Computing the gradient in Eq 4.2, given Eq 4.3, the principal plastic strain rate is

$$\dot{\boldsymbol{\epsilon}}^p = \frac{\dot{\bar{\epsilon}}^p}{2\bar{\sigma}} \begin{bmatrix} 2\sigma_1 - \sigma_2 \\ 2\sigma_2 - \sigma_1 \end{bmatrix} \tag{4.4}$$

Hence, the flow direction is always perpendicular to the yield locus and determined by the stress state. According to Eq 4.4, the principal plastic strain rate ratio is

$$\alpha = \frac{\dot{\epsilon}_2^p}{\dot{\epsilon}_1^p} = \frac{2\sigma_2 - \sigma_1}{2\sigma_1 - \sigma_2} \tag{4.5}$$

The principal plastic strain rate ratio α is thereby only dependent on the present stress state and does not consider the path up to this stress state.

Determination of effective plastic strain $\bar{\epsilon}^p$

The strain rates can be divided into an elastic and a plastic part as $\dot{\boldsymbol{\epsilon}} = \dot{\boldsymbol{\epsilon}}^e + \dot{\boldsymbol{\epsilon}}^p$. In the case of von Mises yield criterion, the effective plastic strain rate can be computed from the principal plastic strain rates

$$\dot{\bar{\epsilon}}^p = \sqrt{\frac{2}{3}(\dot{\epsilon}_1^{p^2} + \dot{\epsilon}_2^{p^2} + \dot{\epsilon}_3^{p^2})} \tag{4.6}$$

Due to plastic incompressibility the volume remains constant, i.e. $\dot{\epsilon}_1^p + \dot{\epsilon}_2^p + \dot{\epsilon}_3^p = 0$. Hence, Eq 4.6 can be rewritten as a function of the in-plane principal plastic strain rates

$$\dot{\bar{\epsilon}}^p = \sqrt{\frac{4}{3}(\dot{\epsilon}_1^{p^2} + \dot{\epsilon}_1^p\dot{\epsilon}_2^p + \dot{\epsilon}_2^{p^2})} \tag{4.7}$$

Furthermore, the effective plastic strain can be obtained by time integration of Eq 4.7

$$\bar{\epsilon}^p = \int \dot{\bar{\epsilon}}^p dt \tag{4.8}$$

Thus, the magnitude of the effective plastic strain can be computed from the in-plane principal plastic strain rates.

4.3 The Marciniak-Kuczynski (M-K) model

This method was developed by Marciniak and Kuczynski in the late 60's and is an established, and presumably the most wide-spread, method for analytical FLC prediction. It was originally developed for prediction of limit strains in the processes of stretch-forming sheet metal, that is to say, to predict limit strains in the right side of the FLD.

The essence of the M-K method is the introduction of an imperfection in the form of a band with reduced sheet thickness, perpendicular to the tensile principal direction. The geometric imperfection is imposed to trigger the plastic instability. The ratio between the sheet thickness inside and outside of the imperfection band is termed the *imperfection factor*. Incipient necking is assumed when the ratio between the first principal strain rate in the neck and the average global first principal strain rate outside of the neck is greater or equal to a preset value k

$$\frac{\dot{\epsilon}_{1,\,\text{neck}}}{\dot{\epsilon}_{1,\,\text{glob}}} \geq k \tag{4.9}$$

When Equation 4.9 is fulfilled the global strains outside the neck is considered to be the sought limit strains. The ratio k will from here on be termed the instability indicator.

For strains in the right part of the FLD, the most critical direction of the imperfection band is perpendicular to the main principal strain direction. However, in the left part of the FLD the angle of the most critical imperfection band varies with the applied strain path. Hence, different angles have to be investigated in order to determine which angle generates the lowest global strains at incipient necking in that specific loading scenario.

The prescribed strains are applied incrementally to the M-K load cell. Initially the relation between the strains inside and outside the imperfection band is equal to the ratio between the thickness outside and inside the imperfection band. This relation remains almost constant up to a point when the strain perpendicular to the neck starts increasing rapidly, while the strain along the imperfection band remains almost constant. This means that the stress state at this point approaches a state corresponding to plane strain. A simplified picture of how the stress inside the neck develops up to the onset of localized necking, in the case of equi-biaxial tension and uniaxial tension, is presented in Figure 4.2.

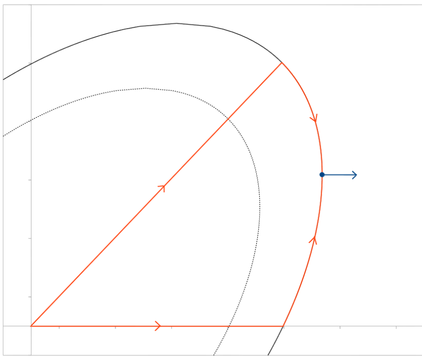

Figure 4.2: *A schematic illustration of the stress state evolution inside the neck for the load cases uniaxial tension and equi-biaxial tension.*

When the ratio between the maximum principal strains reaches the prescribed instability indicator k, a state of incipient necking is assumed to prevail, and the strains outside the neck provides a point to the FLC.

5 Models for failure prediction in metal sheets

5.1 The VCC-model

The VCC-model is based on the observation that fracture is in the majority of cases preceded by plastic instability, i.e. necking. It is thus the necking phenomenon that triggers the subsequent fracture. In this model, plastic instability is considered to be the primary source of failure, and incipient necking is in fact considered to be a failure mechanism in itself. Such an approach is conservative, since it neglects the resistance offered by the material from the incipient necking to the actual fracture. It is still considered to be an acceptable approximation, since in most cases, fracture occurs almost immediately after the formation of a neck.

Compared to the currently used procedure for failure prediction, the following advantages are anticipated by the proposed model

1. Reduced computing time
2. Simplified and less costly material testing
3. No need for a third-party code, eliminating the problems with incompatible program versions
4. No extra cost for the failure prediction code

In the VCC-model, a limit curve for incipient necking serves as a failure criterion. The model assumes an FLC in the principal strain space to be known. Such a curve can be created, either via experiments, or from some theoretical model, e.g. the M-K approach. To be able to take care of the problem with non-linear or broken strain paths, the FLC has to be transformed to a strain path independent variable space, previously discussed in Section 4.2. In the VCC-model the $\alpha - \bar{\varepsilon}^p$ space has been favoured.

As mentioned above, fracture is practically always preceded by necking. There are, however, cases where fracture can occur without any preceding strain localization. One such case is for strain states in the vicinity of pure shear, where in-plane shear fracture is possible. Another case concerns sharp bending deformations, for which fracture can initialize at the sheet surface subjected to tensile strains, and then propagate through the thickness. A third case is for almost equi-biaxial strain states, for which some materials fracture is preceded by necking, while for other materials fracture can occur without any prior strain localization. To account for the above cases, the necking limit curve in the VCC-model is supplemented by two additional limit curves; one taking care of in-plane shear fracture, and another one covering bending fracture.

One or two experimental points have to be known in order to construct the limit curve for bending fracture. The most important point corresponds to fracture in pure bending, and can be determined from a bending test. The other one corresponds to an equi-biaxial strain state, i.e. $\alpha = 1$. This point can only be determined experimentally if fracture does in fact precede necking. Otherwise, this point is of less importance, and could be determined by a clever assumption. The limit curve for bending fracture is approximated by a parabola. The leftmost point of the curve is situated on a vertical line at $\alpha = -0.5$, corresponding to uniaxial tension. This part of the curve is also of less practical importance, since bending fracture is improbable in this strain range.

The limit curve covering in-plane shear fracture is also approximated by a parabola. It is based on one single experimental point, corresponding to fracture in the vicinity of pure shear. The curve is defined by the aforementioned assumed point at $\alpha = -0.5$, the point corresponding to the experimental shear fracture, and finally, an assumption that the curve has its minimum in pure shear, i.e. for $\alpha = -1$.

The three failure curves of the VCC-model are plotted in the same diagram in Figure 5.1, and the properties of the curves are summarized in Table 5.1.

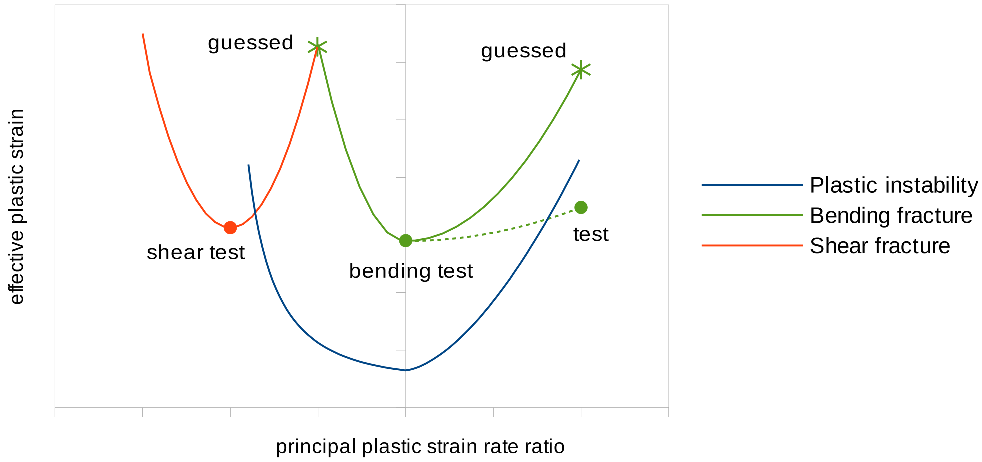

Figure 5.1: *The three failure curves in the VCC model plotted in the* $\alpha - \bar{\epsilon}$ *space*

Curve	Failure mode	Definition range	Failure evaluation surface
1	Plastic instability	$-1 \leq \alpha \leq 1$	Middle integration point
2	Bending fracture	$-0.5 \leq \alpha \leq 1$	Outer integration points
3	Shear fracture	$-1.5 \leq \alpha \leq -0.5$	Middle integration point

Table 5.1: Properties of the three failure curves in the VCC-model.

In FE-simulations element failure is assumed when the current strain state, represented by a point in the $\alpha - \bar{\epsilon}^p$ space, reaches any of the three failure curves. Failure is modelled by removing, also known as eroding, the corresponding element from the simulation.

5.2 The VCC failure criterion implemented in DIEM

The *MAT_ADD_EROSION keyword in LS-DYNA is enabling the connection of one or more separate failure criteria to essentially any material model. Erosion of elements that have satisfied a failure criterion is possible. Within the *MAT_ADD_EROSION framework two failure models are available, who show many similarities and offer great flexibility. These are the GISSMO and DIEM (Damage Initiation and Evolution Model) models. They can both handle DNF and DSF, as well as plastic instability, with different kinds of damage models, or models based on limit curves.

As an alternative to the UMAT implementation of the VCC-model, it has also been implemented in LS-DYNA within the framework of *MAT_ADD_EROSION and the DIEM option. The only difference between the two implementations is that the principal plastic strain rate ratio α in DIEM is calculated in an approximate manner, based on a von Mises yield surface, irrespectively of if some other yield condition or a non-associated flow rule is used. In the current work the material is modelled using a von Mises yield condition, so the above simplification should not influence the results.

Later on in the report whenever DIEM is mentioned it is actually the material model *and* the failure model that is referred to, in this case *MAT_024+DIEM.

5.3 MF GenYld+CrachFEM

MF GenYld+CrachFEM is a sophisticated material and failure model that can be used togheter with a range of commercial explicit FE-codes, such as LS-DYNA, Radioss and ABAQUS/Explicit. The entire product MF GenYld+CrachFEM is generally referred to as just CrachFEM.

The material's plastic behaviour is described by the module MF GenYld (MATFEM generalized yield). This module includes a wide range of yield criteria and models describing isotropic-kinematic and anisotropic hardening. This enables the user to model a variety of different materials.

CrachFEM, not the entire product, is a failure prediction module that accounts for three distinct failure modes; plastic instability, ductile normal fracture and ductile shear fracture.

The *Crach* algorithm, used for prediction of plastic instability, is based on a modified version of the M-K approach. The algorithm predicts instability by solving equlibrium on a submodel, containing a neck, step-by-step increasing the strain until equlibrium is no longer achievable [8]. Exact details about the *Crach* algorithm is difficult to come by, probably because it is considered a company secret at MATFEM.

The user has the possibility to change the interval between activation of the *Crach* algorithm, i.e. how often CrachFEM checks against the instability criterion. Default in CrachFEM is that the algorithm is run when the effective plastic strain has increased by 2 percentage points (p.p.), recommendations from MATFEM is to not go under 1 p.p. in this interval. The *Crach* algorithm is computationally costly, i.e. expensive in terms of computing time, and the simulation time is strongly connected to the activation interval. This is one reason why Volvo Cars is looking for an alternative to CrachFEM.

The ductile normal fracture criterion for shell elements is described in CrachFEM as an analytical function of the stress triaxility η

$$\epsilon^{**}_{\text{eq}}(\eta) = \frac{\epsilon^{+}_{\text{NF}}\sinh(c(\eta^{-}-\eta)) + \epsilon^{-}_{\text{NF}}\sinh(c(\eta-\eta^{+}))}{\sinh(c(\eta^{-}-\eta^{+}))} \tag{5.1}$$

Where $\eta^{+} = 2$ corresponds to equi-biaxial tension and $\eta^{-} = -2$ corresponds to equi-biaxial compression. ϵ^{+}_{NF} is the fracture strain for $\eta = \eta^{+}$, ϵ^{-}_{NF} is the fracture strain for $\eta = \eta^{-}$ and c is a material constant. The fracture strain at compression, ϵ^{-}_{NF} is usually very high due to the fact that normal fracture only occurs under tension.

The ductile shear fracture curve in CrachFEM is defined in the following way

$$\epsilon^{**}_{\text{eq}}(\theta) = \frac{\epsilon^{+}_{\text{SF}}\sinh(f(\theta^{-}-\theta)) + \epsilon^{-}_{\text{SF}}\sinh(f(\theta-\theta^{+}))}{\sinh(f(\theta^{-}-\theta^{+}))} \tag{5.2}$$

Where $\theta^{+} = 2(1-2k_s)$ (equi-biaxial tension), $\theta^{-} = 2(1+2k_s)$ (equi-biaxial compression), ϵ^{+}_{SF} is the fracture strain for $\theta = \theta^{+}$, ϵ^{-}_{SF} is the fracture strain for $\theta = \theta^{-}$, f and k_s are material parameters.

6 Single element simulations

6.1 Introduction

In the single element simulations, 4x4 mm plane stress quad elements with a thickness of 1 mm, were subjected to four different pre-strains, in two separate directions, and up to two different levels of strains. The directions were $\rho_1 = 1$ and $\rho_1 = -1$ and the two strain levels used resulted in effective plastic strains $\bar{\epsilon}^p$ under and above the level corresponding to incipient necking in plane strain.

Figure 6.1 illustrates the four pre-strain cases in the principal strain space, together with a contour curve of constant effective plastic strain corresponding to incipient necking in plane strain.

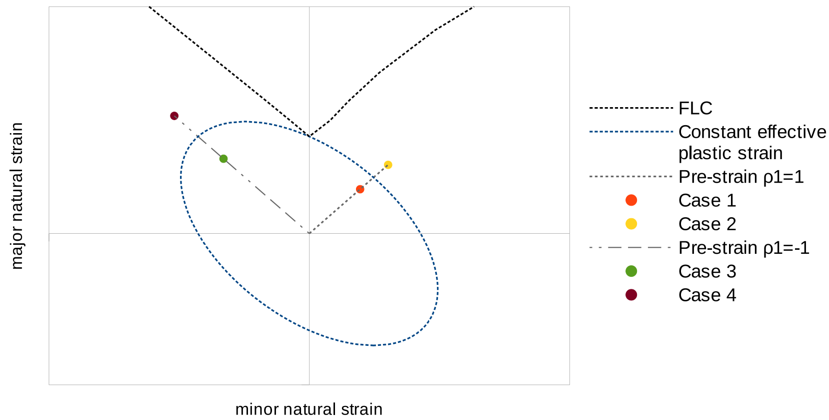

Figure 6.1: *The four pre-strain cases, presented in the principal plastic strain space, together with a curve of constant effective plastic strain corresponding to incipient necking in plane strain.*

From the four states of pre-strains, presented in Figure 6.1, the elements were subjected to 21 strain paths in the interval $\rho_2 \in [-1, 1]$ with increments of 0.1, resulting in 84 different broken strain paths. These strain paths were continued until failure was indicated. The limit strains corresponding to these strain paths are indicated by black dots in Figure 6.2. By connecting these dots a limit strain curve for a specific pre-strain is obtained.

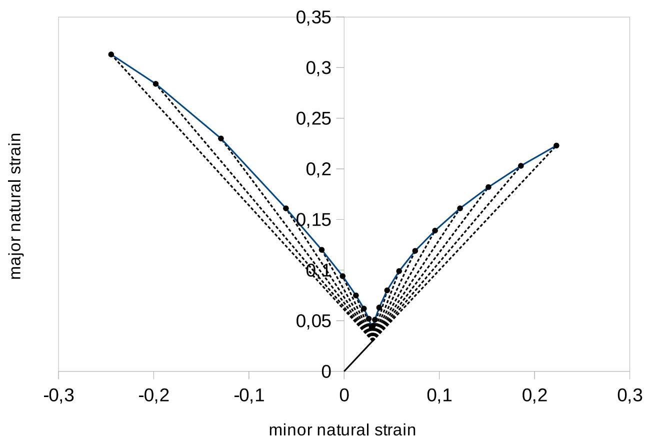

Figure 6.2: *The solid black line is a pre-strain in the direction $\rho_1 = 1$. It is followed by 21 different strain paths, in the interval $\rho_2 \in [-1, 1]$, indicated by the black dashed lines. The black dots are the limit strains for the corresponding broken strain paths.*

6.2 Resulting limit curves and failure modes

The one element simulations have been performed with the three failure models; CrachFEM, DIEM and the VCC-model. The resulting limit curves, presented in the principal strain space and the $\alpha - \bar{\epsilon}^p$ space, indicated by the three models are plotted in Figures 6.3-6.6. Unless otherwise stated all CrachFEM simulations are done with a *Crach* algorithm interval activation of 2 p.p. increase in effective plastic strain.

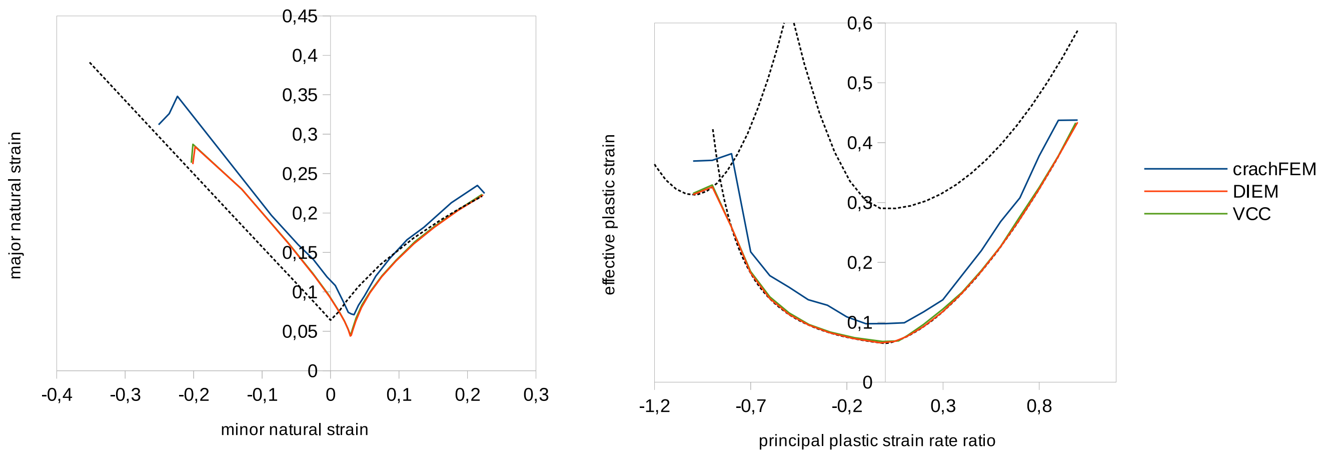

(a) *The principal strain space* (b) *The $\alpha - \bar{\epsilon}^p$ space*

Figure 6.3: *Limit curves in pre-strain case 1 ($\rho_1 = 1$, small pre-strain).*

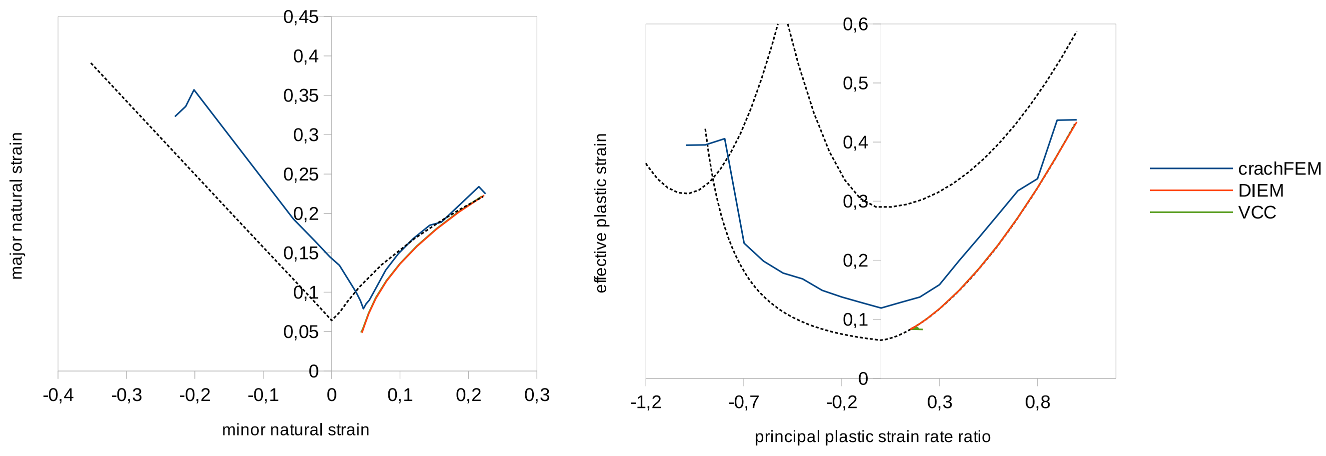

(a) *The principal strain space* (b) *The $\alpha - \bar{\epsilon}^p$ space*

Figure 6.4: *Limit curves in pre-strain case 2 ($\rho_1 = 1$, large pre-strain).*

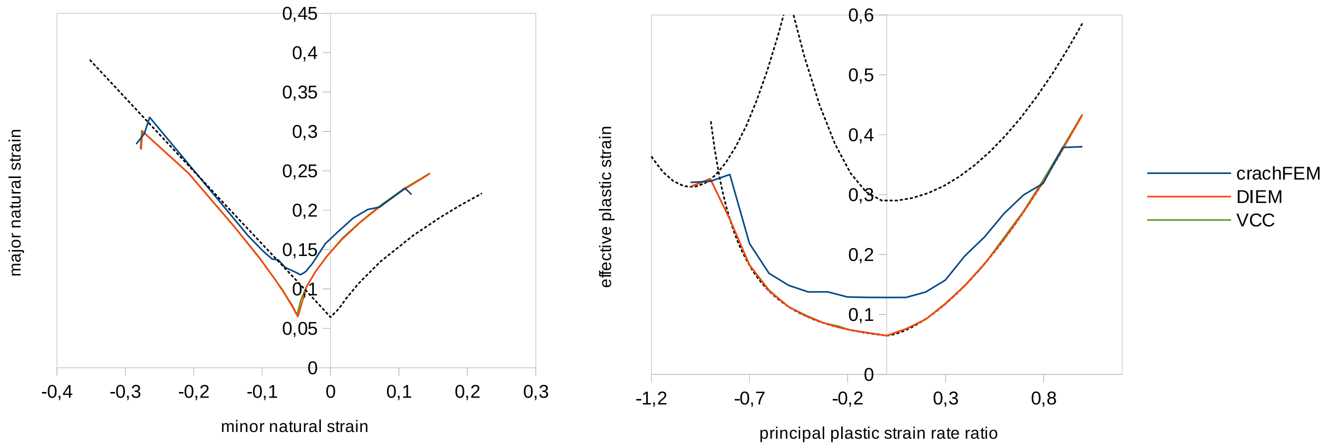

(a) *The principal strain space* (b) *The* $\alpha - \bar{\varepsilon}^p$ *space*

Figure 6.5: *Limit curves in pre-strain case 3 ($\rho_1 = -1$, small pre-strain).*

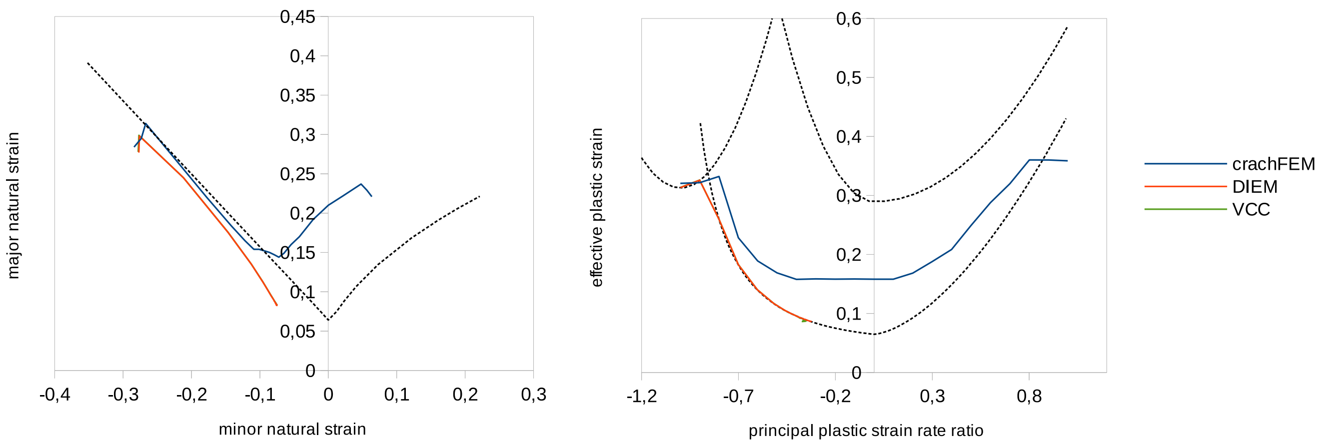

(a) *The principal strain space* (b) *The* $\alpha - \bar{\varepsilon}^p$ *space*

Figure 6.6: *Limit curves in pre-strain case 4 ($\rho_1 = -1$, large pre-strain).*

The failure modes indicated by the three models for all strain paths are summarized in Table 6.1.

	CrachFEM				**DIEM**				**VCC-model**			
Pre-strain case	1	2	3	4	1	2	3	4	1	2	3	4
$\rho_2 = -1$	DSF	DSF	DSF	DSF	DSF	P.I.	DSF	DSF	DSF	P.I.	DSF	DSF
$\rho_2 = -0.9$	DSF	DSF	DSF	DSF	DSF	P.I.	DSF	DSF	DSF	P.I.	DSF	DSF
$\rho_2 = -0.8$	DSF	DSF	DSF	DSF	P.I.	P.I.	P.I.	P.I.	P.I.	P.I.	P.I.	P.I.
$\rho_2 \in [-0.7, 1]$	P.I.	P.I.	P.I.	P.I.	P.I.	P.I.	P.I.	P.I.	P.I.	P.I.	P.I.	P.I.

Table 6.1: Failure modes indicated by the three models; plastic instability (P.I.) and ductile shear fracture (DSF).

6.3 Investigation of the Crach algorithm activation interval

As previously mentioned in Section 5.3 the *Crach* algorithm for necking prediction is only activated at certain instances in time, determined by a prescribed interval of increase in $\bar{\epsilon}^p$. Intervals of 0.5, 1 and 2 p.p. increase in effective plastic strain were examined. The activation interval was deliberately set below the recommendation from MATFEM to get an idea of the motivation behind this recommendation. Limit strains in the four pre-strain cases are presented in Figures 6.7-6.10.

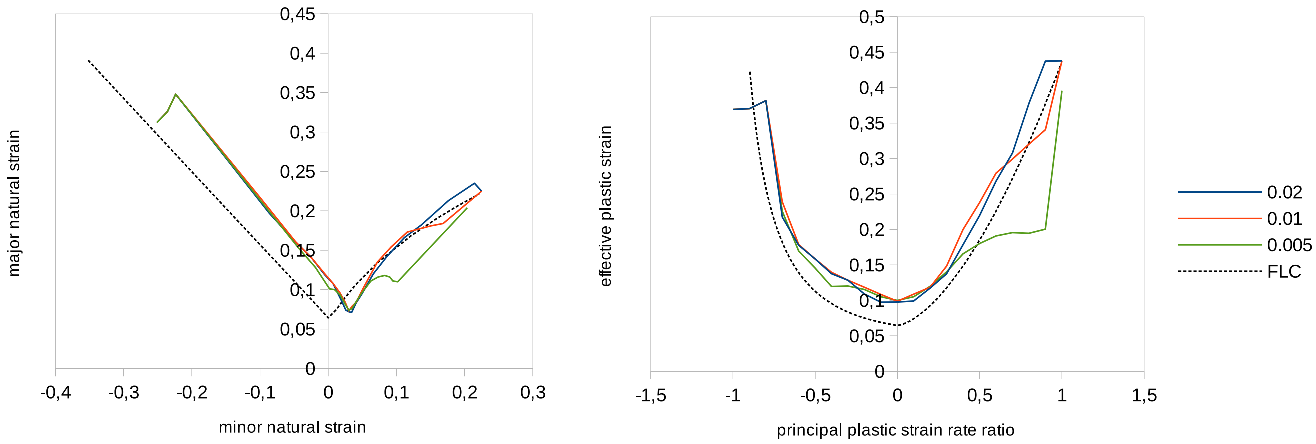

(a) *The principal strain space* (b) *The $\alpha - \bar{\epsilon}^p$ space*

Figure 6.7: *Three different intervals between activation of the Crach algorithm in pre-strain case 1.*

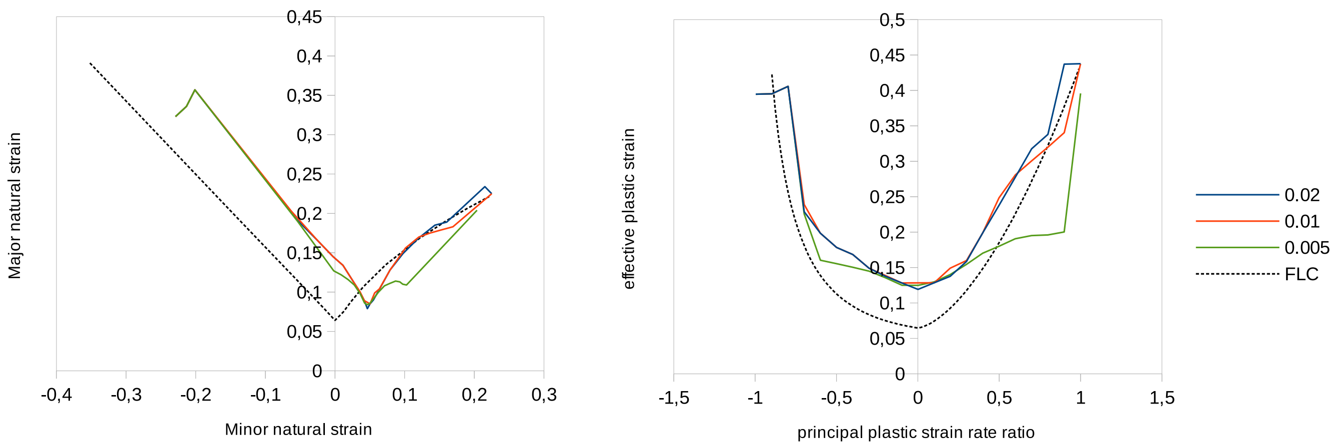

(a) *The principal strain space* (b) *The $\alpha - \bar{\epsilon}^p$ space*

Figure 6.8: *Three different intervals between activation of the Crach algorithm in pre-strain case 2.*

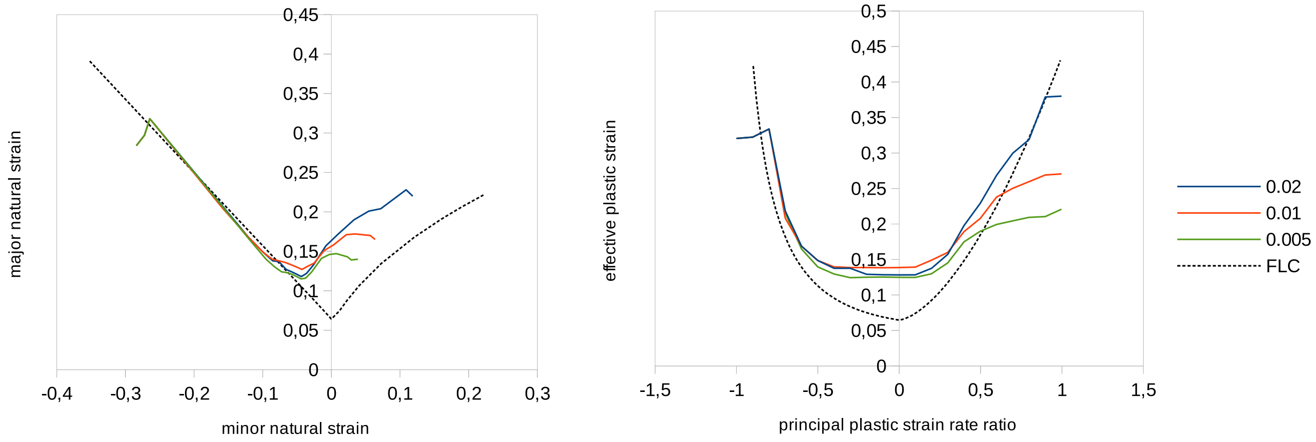

(a) *The principal strain space* (b) *The $\alpha - \bar{\epsilon}^p$ space*

Figure 6.9: *Three different intervals between activation of the Crach algorithm in pre-strain case 3.*

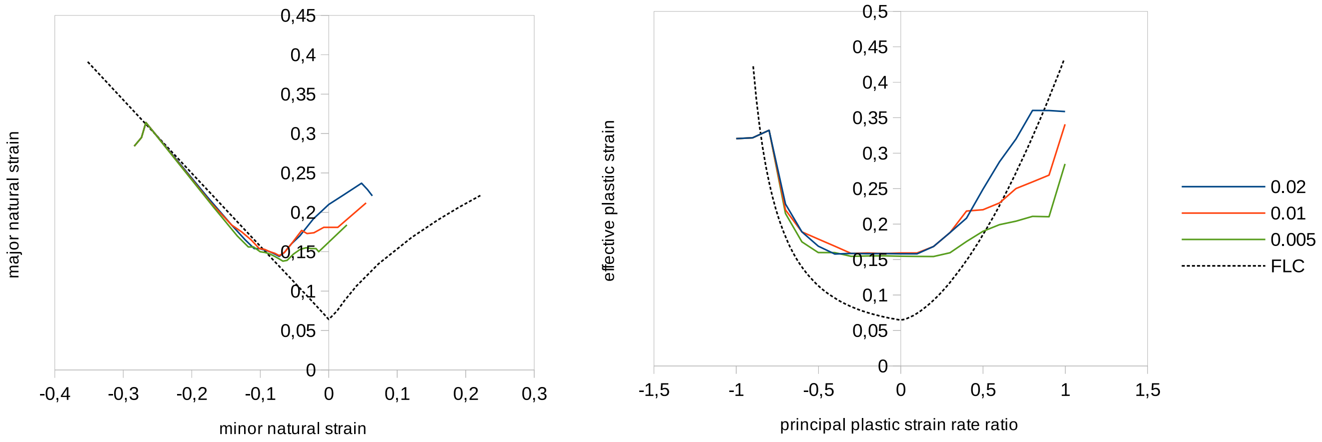

(a) *The principal strain space* (b) *The $\alpha - \bar{\epsilon}^p$ space*

Figure 6.10: *Three different intervals between activation of the Crach algorithm in pre-strain case 4.*

6.4 Observations and analyses of findings

The VCC-model and DIEM seem to yield identical results, indicating that the implementation in DIEM is correct, and that DIEM could be used as a sufficient alternative to the user implementation of the VCC-model.

Linear strain path simulations performed alongside the main simulations revealed that the plastic instability limit curves indicated by CrachFEM conforms to the FLC. This is hardly surprising, since the FLC in the VCC-model is reversed engineered from CrachFEM [2]. The interesting thing surfaces when broken strain paths are applied, in which case the limit curves indicated by the VCC-model still correspond to the FLC in the $\alpha - \bar{\epsilon}^p$ space, while the curves predicted by CrachFEM do not. For small pre-strains there are noticeable, but not dramatic differences in results between CrachFEM and the VCC-model. However, for large pre-strains the differences are greater.

Analyzing Figures 6.3-6.6 it seems the more effective plastic strain accumulated in a particular pre-strain direction the more forgiving CrachFEM is in terms of the allowed effective plastic strain prior to plastic instability indication. This hypothesis was tested by applying an even higher pre-strain than that in pre-strain case 4, this is termed pre-strain case X. The limit curves indicated by CrachFEM in pre-strain case 3, 4 and X are plotted in Figure 6.11.

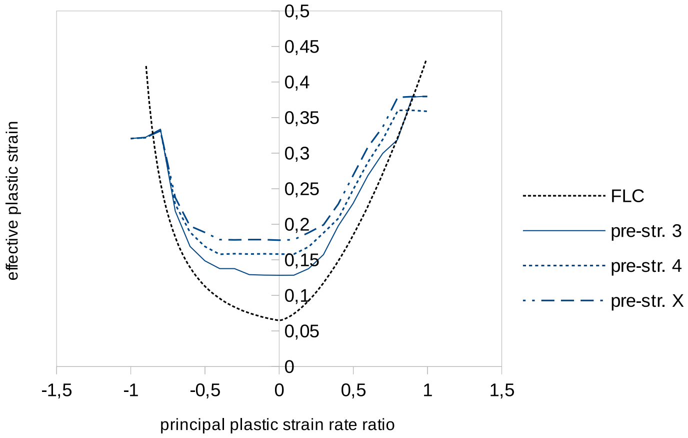

Figure 6.11: *The limit curves indicated by CrachFEM in the one element simulations in pre-strain case 3, 4 and X.*

Figure 6.11 confirms that the higher the pre-strain is in the direction $\rho_1 = -1$ the higher the limit curve rises in the $\alpha - \bar{\epsilon}^p$ space. One element simulations with a pre-strain $\rho_1 = -2$, up to the same $\bar{\epsilon}^p$ as in pre-strain case 4, revealed that the limit curve was elevated beyond the limit curve predicted in pre-strain case 4. This implies that the $\bar{\epsilon}^p$ tolerated by CrachFEM before plastic instability indication is dependent on both the direction and magnitude of the pre-strain.

In Table 6.1 it is evident that necking is the dominating failure mode, within the strain ranges covered in this investigation. The results for DIEM and the VCC-model are what can be expected from the appearances of the failure curves. CrachFEM shows a slightly bigger tendency to indicate shear failure than the other two models.

For sudden changes in direction of the strain path, there is an instantaneous change in α, but no change in $\bar{\epsilon}^p$. The VCC- model often indicates an immediate failure in such cases, but CrachFEM does not, since it can only predict failure if there is a substantial increase in $\bar{\epsilon}^p$. It should be emphasized that these disparities are only present if there is a *continuous* strain path. If there is an unloading between the first and the second linear path, no failure is indicated at the start of the second part. These matters have previously been discussed in [2].

The particular study of CrachFEM indicates that the limit strains are significantly influenced by the size of the *Crach* algorithm activation interval. This is an unpleasant observation, since CrachFEM is the currently used tool for failure prediction in car crash simulations at Volvo Cars. It was initially assumed that if the *Crach* algorithm activation interval was decreased one would detect a lowering of $\bar{\epsilon}^p$ corresponding to the size of the activation interval, Figures 6.7-6.10 indicates that this was not the case.

7 Crash box simulations

7.1 Introduction

Crash boxes are usually constructed from ductile materials, such as aluminium alloys. However, in this case the box was modelled with the same boron steel as in the previous simulations. Since it was the material models, and not the actual crash box itself, that were evaluated this did not cause any problem. The crash box was discretized using 22,775 Belytschko-Tsay elements with a thickness of 1 mm. The mesh is depicted in orange in Figure 7.1.

The axial deformation of the crash box was accomplished by simulating three separate vertical drops of a 75 kg rigid plate, depicted in green in Figure 7.1, from heights of 1.27 m, 2.87 m and 5.10 m. In this section these will be referred to as three separate load cases; load case #1, #2 and #3, respectively.

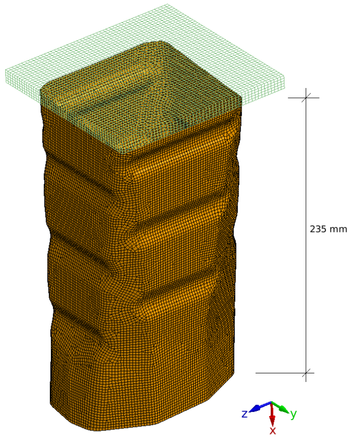

Figure 7.1: *The mesh of the crash box in orange, together with the rigid plate in green. The initial length of the crash box was 235 mm*

The reaction force in the interface between the rigid plate and the crash box was calculated via the x-acceleration of the rigid plate. The axial displacement was also determined via the movement of the rigid plate, taking into account the fact that the plate was initially not in contact with the crash box. The absorbed internal energy was obtained by numerical integration of the force-displacement curve. The integration rule employed was the trapezoidal method.

The elastic spring-back was computed by determining the points in time where the axial displacement had its maximum, and the reaction force was zero. The difference in displacement between these two point were considered to be the elastic spring-back.

Furthermore, the models were also compared with respect to simulation time and element erosion. Both the evolution of the element erosion and the number of elements eroded in different modes were investigated. Not only the number of eroded elements are of interest, but also the regions from which the elements are eroded are of interest, in order to detect potential differences in model behaviour. This investigation was carried out by gathering the ID's of the eroded elements, from the *d3hsp* files, into sets. Matlab was then used to find the common members of these element sets.

7.2 Axial deformation and simulation time

The deformations of the crash box at the last time step, after the elastic spring-back, in the three load cases are shown in Figures 7.2-7.4.

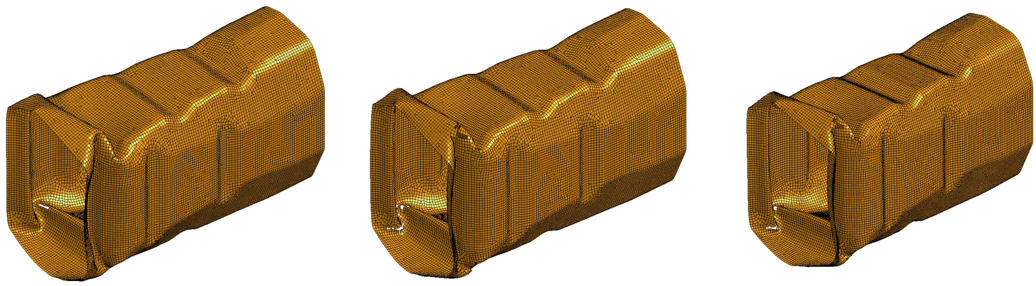

(a) *CrachFEM* (b) *DIEM* (c) *VCC-model*

Figure 7.2: *The deformation of the crash box, as suggested by the three models, in load case #1.*

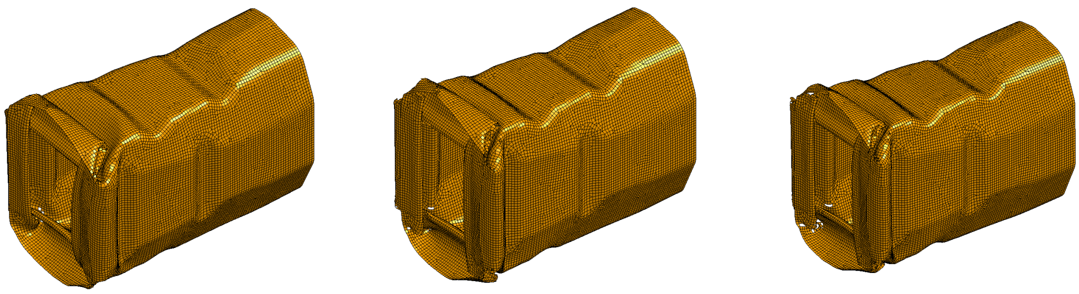

(a) *CrachFEM* (b) *DIEM* (c) *VCC-model*

Figure 7.3: *The deformation of the crash box, as suggested by the three models, in load case #2.*

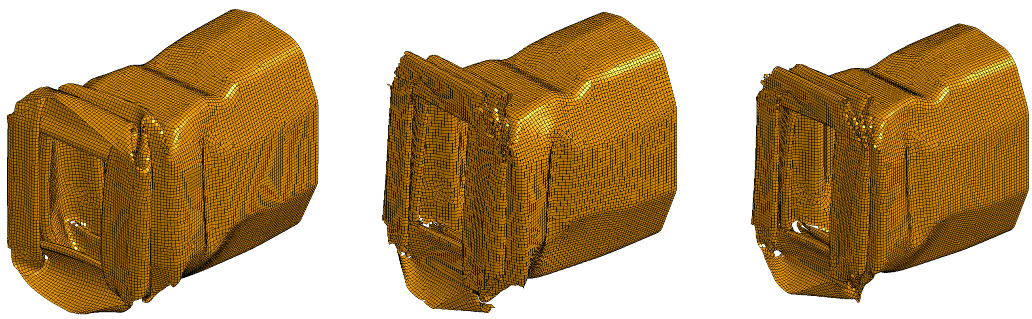

(a) *CrachFEM* (b) *DIEM* (c) *VCC-model*

Figure 7.4: *The deformation of the crash box, as suggested by the three models, in load case #3.*

Since CrachFEM is currently used at Volvo Cars that model will be used as the reference. The simulation times, both absolute and relative to CrachFEM, used by the three models in the three load cases are presented in Table 7.1.

	CrachFEM	**DIEM**	**VCC-model**
Load case #1	1h 23m 43s (100%)	0h 48m 27s (57.9%)	1h 10m 46s (84.5%)
Load case #2	1h 59m 27s (100%)	1h 6m 17s (55.5%)	1h 33m 58s (78.7%)
Load case #3	2h 31m 50s (100%)	1h 25m 2s (56%)	1h 57m 39s (77.5%)

Table 7.1: Simulation time used by the three models in the three load cases.

Plotted in Figure 7.5 are the axial compression distances of the crash box in the three load cases.

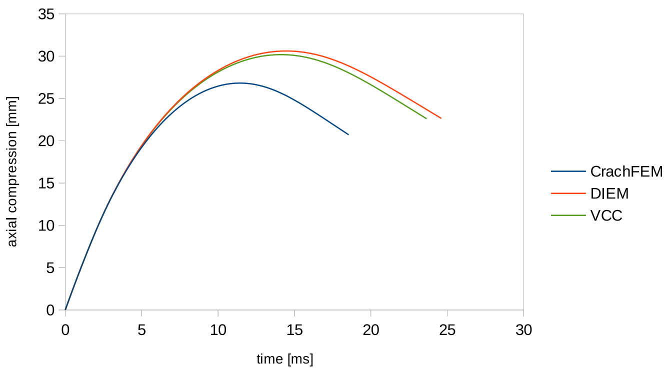

(a) *Load case #1.*

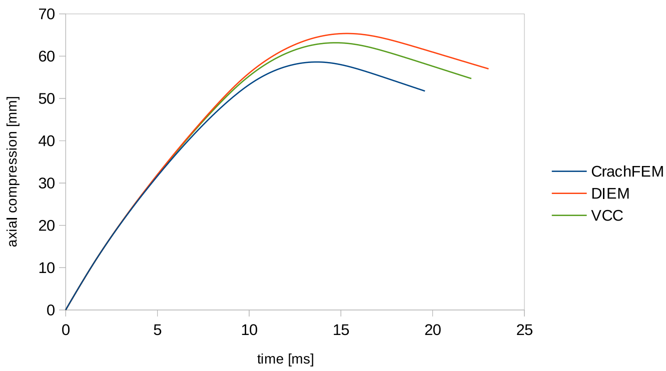

(b) *Load case #2.*

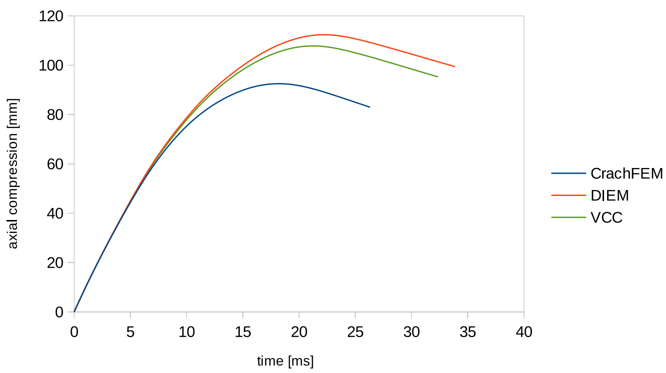

(c) *Load case #3.*

Figure 7.5: *The axial compression of the crash box in the three load cases.*

The total elastic spring-back of the crash box, S_b, in the three different load cases, are presented in Table 7.2 below.

	CrachFEM	**DIEM**	**VCC-model**
Load case #1	$S_b = 6.11\,mm$	$S_b = 7.96\,mm$	$S_b = 7.48\,mm$
Load case #2	$S_b = 6.90\,mm$	$S_b = 8.38\,mm$	$S_b = 8.04\,mm$
Load case #3	$S_b = 9.61\,mm$	$S_b = 12.94\,mm$	$S_b = 11.04\,mm$

Table 7.2: Elastic spring-back of the crash box in the three load cases.

7.3 Reaction force and absorbed energy

Illustrated in Figures 7.6-7.8 are the force-displacement curves and the energy absorbed by the crash box during the axial collapse, in the three load cases. The absorbed energy curves on the right have been numerically integrated from the force-displacement curves on the left.

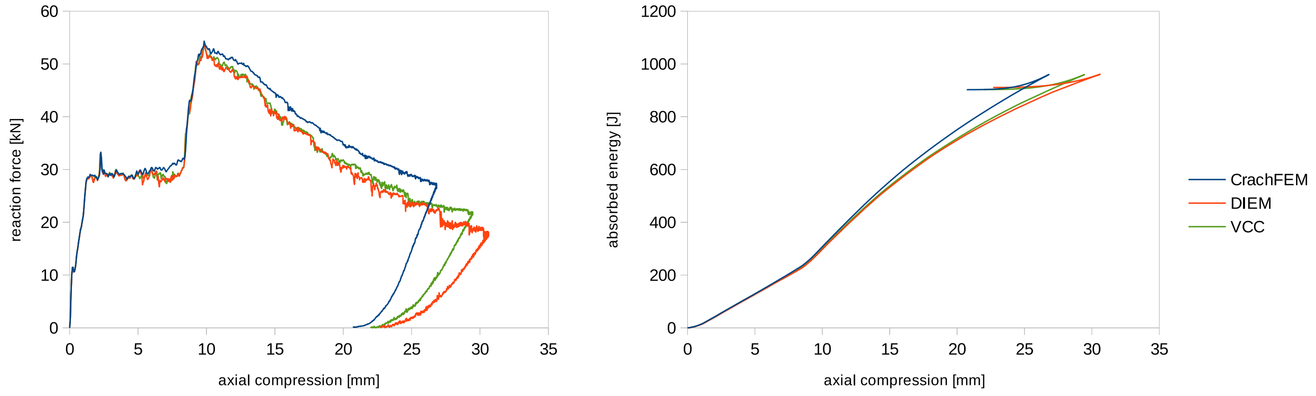

(a) (b)

Figure 7.6: *Force-displacement (a) and energy-displacement (b) curves in load case* #1.

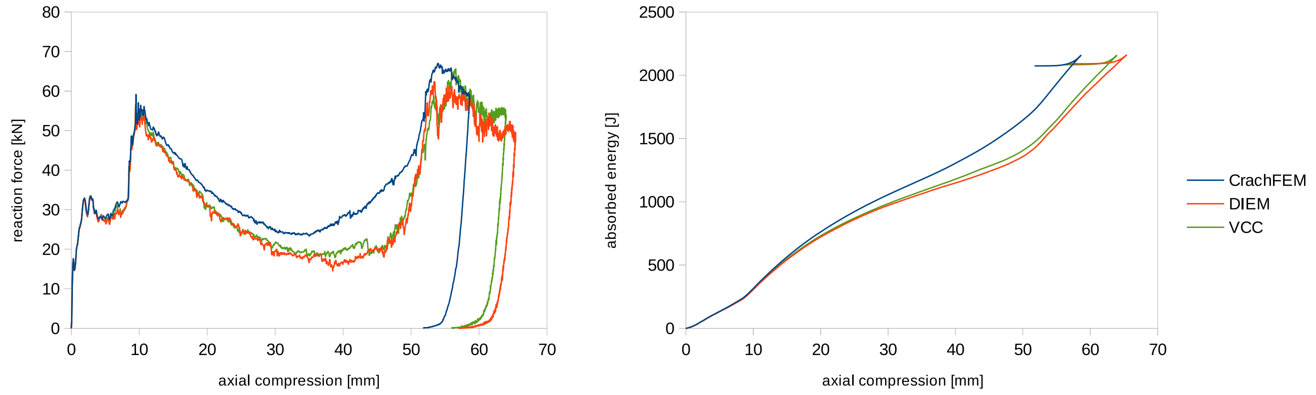

(a) (b)

Figure 7.7: *Force-displacement (a) and energy-displacement (b) curves in load case* #2.

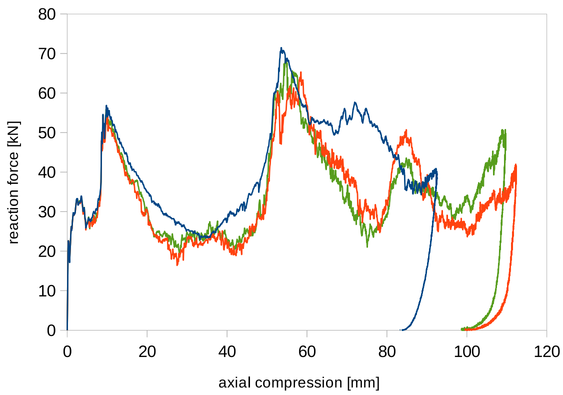

(a)

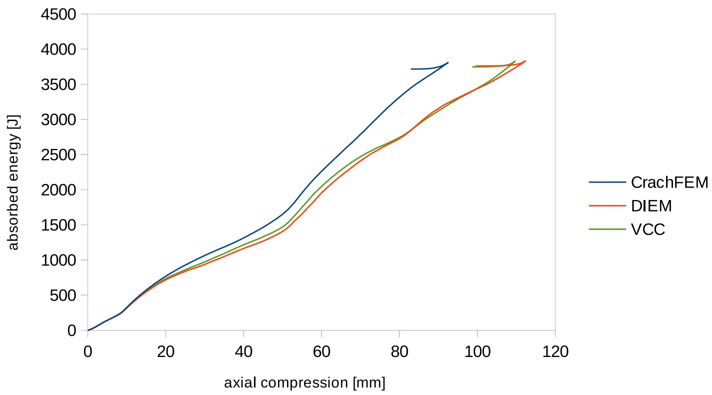

(b)

Figure 7.8: *Force-displacement (a) and energy-displacement (b) curves in load case #3.*

7.4 Element erosion

The three models did not erode the same number of elements and the elements that were eroded were removed from the structure at different points in time. The evolution of the element erosion is illustrated in Figure 7.9.

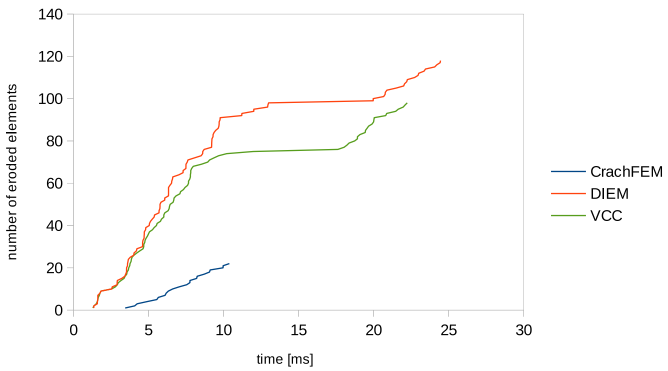

(a) *Load case #1.*

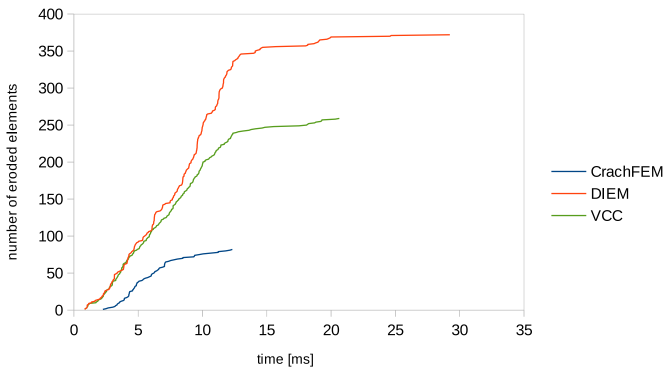

(b) *Load case #2.*

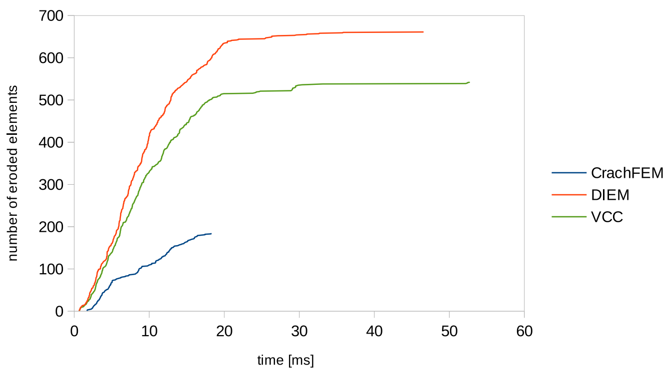

(c) *Load case #3.*

Figure 7.9: *The evolution of the element erosion in the three different load cases.*

The total number of elements eroded by the models are presented in Table 7.3.

	CrachFEM	DIEM	VCC-model
Load case #1	22 (0.10%)	118 (0.52%)	98 (0.43%)
Load case #2	82 (0.36%)	371 (1.63%)	259 (1.14%)
Load case #3	184 (0.81%)	661 (2.90%)	543 (2.38%)

Table 7.3: The total number of elements eroded in the three load cases.

The distribution of the number of eroded elements between the three failure modes are presented in Table 7.4.

	CrachFEM			DIEM			VCC-model		
	P.I.	DNF	DSF	P.I.	Bend.	DSF	P.I.	Bend.	DSF
Load case #1	0 (0%)	22 (100%)	0 (0%)	50 (42.4%)	61 (51.7%)	7 (5.9%)	42 (42.9%)	55 (56.1%)	1 (1.0%)
Load case #2	3 (3.7%)	78 (95.1%)	1 (1.2%)	119 (32.1%)	235 (63.3%)	17 (4.6%)	86 (33.2%)	157 (60.6%)	16 (6.2%)
Load case #3	13 (7.1%)	166 (90.2%)	5 (2.7%)	210 (31.8%)	418 (63.2%)	33 (5.0%)	175 (32.2%)	341 (62.8%)	27 (5.0%)

Table 7.4: Distribution of the eroded elements between the three failure modes.

Analyzes of the number of eroded elements shared by the three models, in the three load cases, have been performed. In other words; the cardinality ($|\bullet|$) of the intersections of the sets of eroded elements, displayed in Figure 7.10, have been calculated. The findings are presented in Tables 7.5 and 7.6.

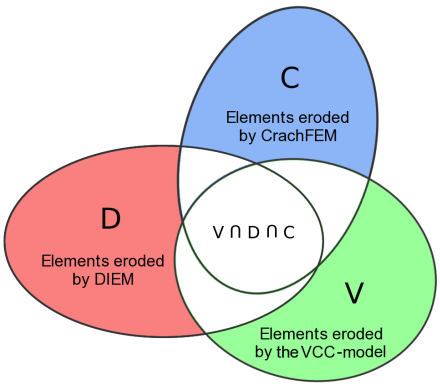

Figure 7.10: *A principle Venn diagram of the sets of elements eroded by the three models.*

Table 7.5 shows the cardinality of the intersections between the three sets of eroded elements displayed in Figure 7.10. The mode in which the elements failed were not taken into consideration here.

	$\lvert\mathbf{C}\cap\mathbf{D}\rvert$	$\lvert\mathbf{C}\cap\mathbf{V}\rvert$	$\lvert\mathbf{D}\cap\mathbf{V}\rvert$	$\lvert\mathbf{V}\cap\mathbf{D}\cap\mathbf{C}\rvert$
Load case #1	9	7	79	6
Load case #2	43	49	190	34
Load case #3	81	71	351	57

Table 7.5: The cardinality of the intersections between the sets of eroded elements.

A more detailed study was carried out where the sets of eroded elements were sorted into subsets containing the elements eroded in each mode, e.g. for CrachFEM one gets $C = \{C_{P.I.}, C_{DNF}, C_{DSF}\}$. Presented in Table 7.6 are the number of elements shared by the models in each failure mode.

	$\lvert \mathbf{C_M} \cap \mathbf{D_M} \rvert$			$\lvert \mathbf{C_M} \cap \mathbf{V_M} \rvert$			$\lvert \mathbf{D_M} \cap \mathbf{V_M} \rvert$			$\lvert \mathbf{V_M} \cap \mathbf{D_M} \cap \mathbf{C_M} \rvert$		
Mode, **M**=	P.I.	DNF	DSF	P.I.	DNF	DSF	P.I.	Bend.	DSF	P.I.	DNF	DSF
Load case #1	0	7	0	0	4	0	33	38	1	0	3	0
Load case #2	0	33	0	0	38	0	55	96	6	0	25	0
Load case #3	3	61	1	2	57	1	82	190	4	1	43	0

Table 7.6: The cardinality of the intersections between the sets of eroded elements in each failure mode, in the three load cases.

7.5 Observations and analyses of findings

Figure 7.5 reveals that the deformations of the crash boxes were initially similar in all three load cases, when comparing the three models. This resemblance is also reflected in the force-displacement curves plotted in Figures 7.6-7.8. However, later on in the simulations the deformation field deviates, this is especially distinguishable in load case #3. This could be explained by the evolution of the element erosion, plotted in Figure 7.9, where it is observable that DIEM and the VCC-model eroded more elements, and with a higher frequency, than CrachFEM. Moreover, the element erosion frequency in DIEM and the VCC-model were similar, but DIEM ended up eroding around 20% more elements than the VCC-model in load case #3. The variation in element erosion can also explain the differences in axial compression distances; fewer eroded elements results, as one might expect, in a stiffer structure. This goes hand in hand with the general pattern seen in the calculated spring-backs in Table 7.2 as well.

User implemented material models have previously shown tendencies to be less efficient than commercial material models in LS-DYNA. This fact coincides with what was observed in the crash box simulations, where *MAT_024+DIEM was consistently faster than the VCC-model in all three load cases.

The most remarkable in Table 7.4 is that CrachFEM has eroded proportionally fewer elements in the plastic instability mode when comparing to DIEM and the VCC-model. The answer to this was searched for by focusing on two elements that DIEM and the VCC-model shared in the plastic instability mode in load case #3, but CrachFEM did not erode at all. Elements that were eroded early in the simulation were chosen to circumvent the issue that the crash box deformation fields differed between the three model. Strain paths, in the principal strain space and the $\alpha - \bar{\epsilon}^p$ space, in these elements are plotted i Figures 7.11-7.12.

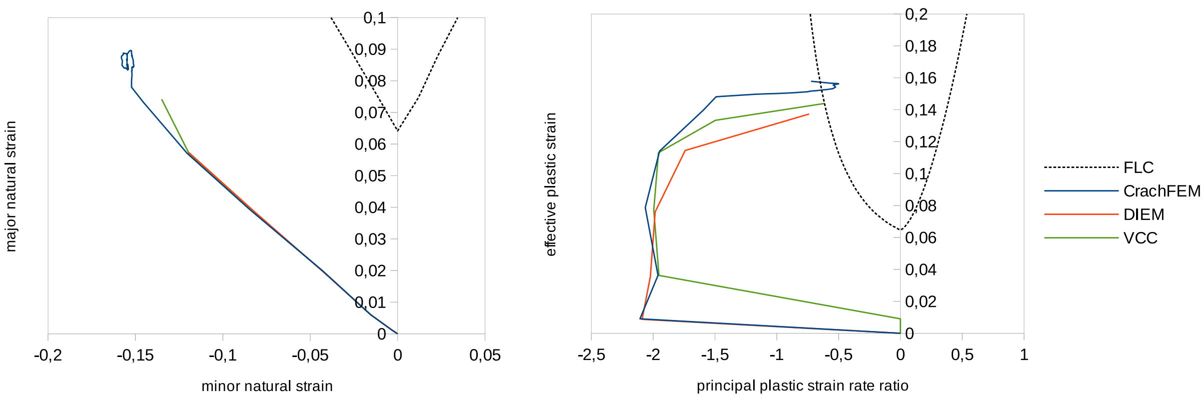

(a) *The principal strain space*

(b) *The $\alpha - \bar{\epsilon}^p$ space*

Figure 7.11: *Strain paths in one of the elements (66473) that DIEM and the VCC-model shared in the plastic instability mode, but CrachFEM did not erode.*

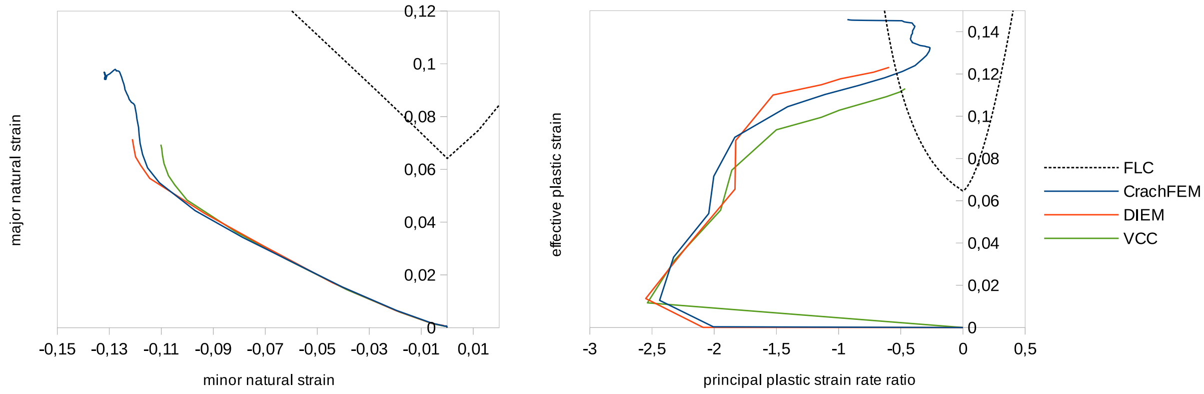

(a) *The principal strain space* (b) *The $\alpha - \bar{\epsilon}^p$ space*

Figure 7.12: *Strain paths in one of the elements (12965) that DIEM and the VCC-model shared in the plastic instability mode, but CrachFEM did not erode.*

Figures 7.11-7.12 shows that the strain paths in the two examined elements are rather similar independently of the model used. This indicates that the material part of the material models behaves similarly, but the failure parts does not. The two elements were eroded by DIEM and the VCC-model on the inputted instability curve, but CrachFEM did not take notice of this failure curve (note that this curve is *not* an input in CrachFEM). Analogous observations can be done in the broken strain path one element simulations, where the limit curves indicated by CrachFEM were constantly situated above those indicated by DIEM and the VCC-model.

To further investigate why CrachFEM eroded such a low number of elements in the plastic instability mode, the position in the $\alpha - \bar{\epsilon}^p$ space of the elements eroded by CrachFEM and the VCC-model in load case #3 are plotted in Figure 45.

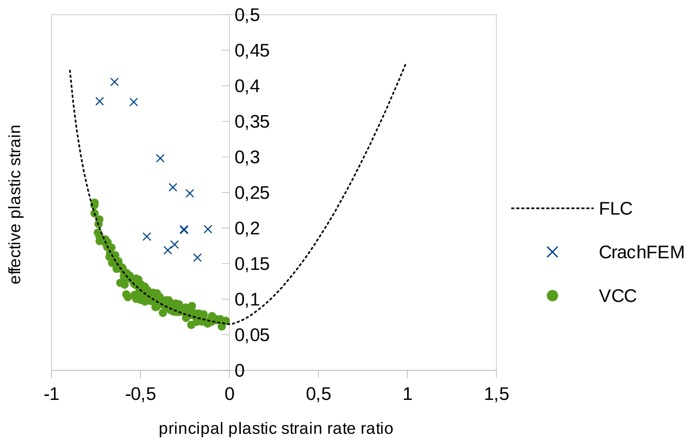

Figure 7.13: *α and $\bar{\epsilon}^p$ in the elements that were eroded in the plastic instability mode in CrachFEM and the VCC-model.*

Figure 7.13 reveals, yet again, that $\bar{\epsilon}^p$ in the elements eroded by CrachFEM in the plastic instability mode is much higher, for a given α, than in the VCC-model. This indicates that the *Crach* algorithm in CrachFEM has increased the effective plastic strain limit corresponding to plastic instability, based on the strain path in the element. Similar behaviour was displayed by the one element simulations comparing pre-strain case 3, 4 and X, as was discussed in Section 6.4. This fact might explain why CrachFEM eroded very few elements in the plastic instability mode.

The observations from Figures 7.11-7.12 sparked the idea to deactivate the failure prediction modules to see if similar results were obtained with CrachFEM, DIEM and the VCC-model. The axial compression and reaction force in load case #3, with no failure active, are plotted in Figure 7.14.

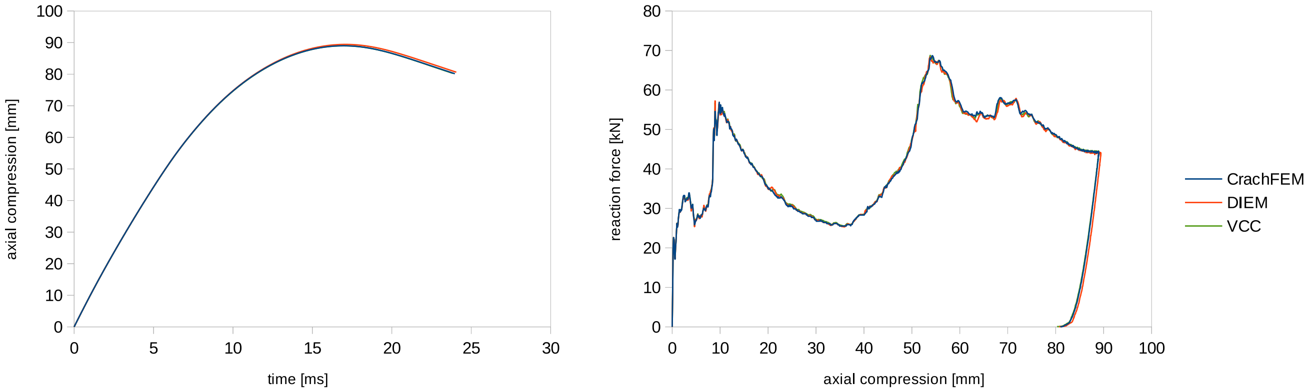

(a) *Axial compression distance*

(b) *Force-displacement curve*

Figure 7.14: *Axial compression distance and force-displacement curves in load case #3, with no failures active.*

Figure 7.14 provides a clear indication that the model differences observed in Figures 7.5-7.9 are entirely caused by the way the models predict failure, and ultimately erodes elements. This runs counter to the single element simulation results, where DIEM and the VCC-model exhibited no difference in failure prediction behaviour.

In the VCC-model stresses and strains are extrapolated to the shell element surface from the outer-most integration point. Thus, when Gauss quadrature is used in DIEM the 'surface' stresses and strains are not evaluated in the same location as in the VCC-model. Therefore, the Lobatto integration scheme was adopted, which has integration points on the element surface.

The change in integration scheme caused all three models to erode more elements and the difference between the models remained. The increase in element erosion was not surprising since stresses and strains are higher closer to the surface of the element during bending deformation. What was surprising, though, was that the VCC-model exhibited this behaviour, since the aforementioned extrapolation is done. Some variation might be expected, but not to the extend that was observed.

8 Full scale car crash simulations

8.1 Introduction

The full scale car crash simulations were performed in two separate load cases, on Volvo Cars' computer cluster. The implementation of the VCC-model together with MF GenYld+CrachFEM in LS-DYNA caused complications, hence only CrachFEM and DIEM were compared in these simulations.

Currently on Volvo Cars CrachFEM is only used to model materials in parts where risk of failure is assumed, this is done to reduce the simulation time. CrachFEM is not exclusively used to model boron steel but also other steels, various plastics and aluminium.

Presented in Table 8.1 are the percentage of plastic and aluminum shell elements modelled with CrachFEM and the proportion of replaced CrachFEM steel shell elements, i.e. all steels modelled with CrachFEM were replaced.

	Load case 1	**Load case 2**
Plastic & Al	13.3%	15.7%
Replaced steel	9.5%	3.7%

Table 8.1: Percentage of plastic and aluminium CrachFEM shell elements remaining, and the percentage of replaced CrachFEM steel shell elements, in the two load cases.

The simulation where CrachFEM was used to model the steels was considered the reference, against which the presented results are normalized. The material in the heat affected zone (HAZ), around the spot-welds, was modelled with the same boron steel used in rest of this study, earlier described in Section 2.2. No care has been taken to what base materials that are weld togheter. This is a major simplification of reality, where of course the properties of the heat affected zone is highly affected by the base material properties.

The total simulation time in the four simulations was extracted from the *d3hsp* files. The *Timing information*, i.e. the CPU time used by specific processes in the simulations, was also investigated. The initial guess was that most of the time, if any, would be won on the element processing. In addition, the reference was checked for cracks and compared to the results from simulations where DIEM was used to model the steels.

Since all steels has been replaced by one and the same boron steel it is counter productive to investigate the reason for possible differences, in reality there are a large number of different steel alloys in the car.

8.2 Results

The relative simulation time in the full scale car crash simulations are presented in Table 8.2.

	Load case 1	**Load case 2**
Reference	100%	100%
DIEM	92.9%	98.3%

Table 8.2: The relative simulation time in the full scale car crash simulations, in the two load cases.

Presented in Table 8.3 are the relative CPU time used by two of the most time consuming processes.

	Load case 1		**Load case 2**	
	Refer.	DIEM	Refer.	DIEM
Shell element processing	27.63%	23.81%	15.29%	14.04%
Contact algorithm	37.85%	36.82%	30.78%	31.00%

Table 8.3: Percentage of the total CPU time used by two of the most time consuming processes.

Figure 8.1 shows a region in which the reference model and the DIEM model diverge from one another regarding size and occurrence of cracks, in load case 1.

(a) *Undeformed geometry*

(b) *Reference in load case 1*

(c) *DIEM in load case 1*

Figure 8.1: *A region in the car, undeformed and deformed, in load case 1.*

Figure 8.2 depicts a region where DIEM behaves differently, when compared to the reference model, in the heat affected zones around the spot-welds, in load case 2.

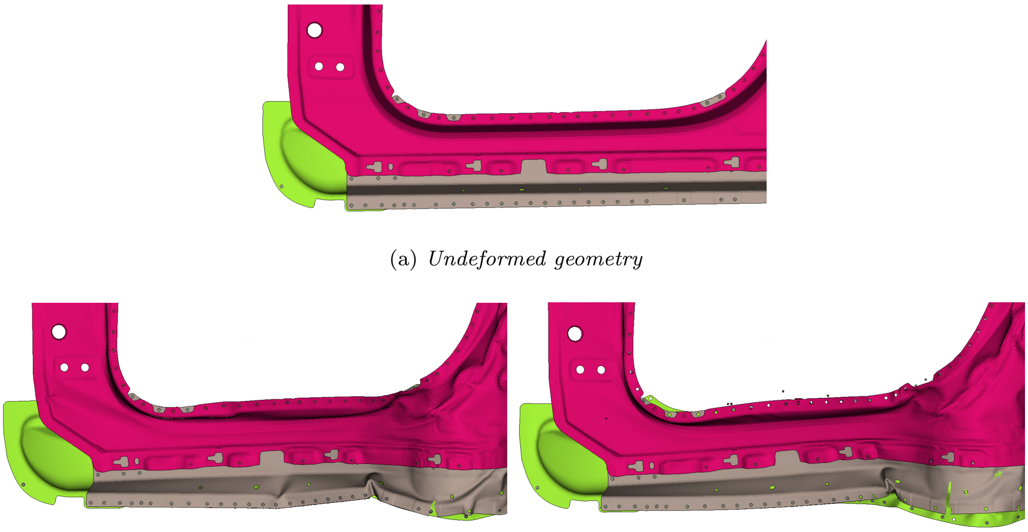

(a) *Undeformed geometry*

(b) *Reference in load case 2*

(c) *DIEM in load case 2*

Figure 8.2: *A region in the car, undeformed and deformed, in load case 2.*

8.3 Observations and discussion

To explain the relatively low decrease in simulation time, in load case 1, one can probably refer to the fact there were 40% more plastic and aluminium CrachFEM elements remaining than steel elements replaced. Furthermore, the remaining CrachFEM elements were situated in regions where a lot of cracking occurred, i.e. those elements caused the time consuming *Crach* algorithm to be activated regularly. The even lower time gain in load case 2 could be explained by the same fact. However, in this case it was even more pronounced, with 4.2 times more CrachFEM elements left than replaced.

The initial hypothesis that the time gain, although it was rather modest, would be won on the processing of the shell elements seems to have been confirmed when studying Table 8.3.

Looking at Figure 8.1 it is obvious that DIEM has suggested a crack in a part where CrachFEM has not. There are one crack that coincides spatially, in the studied region, but DIEM predicted the crack to grow much further. This behaviour was observed in the crash box simulations as well, where DIEM consistently eroded more elements than CrachFEM.

A general observation from the full scale car crash simulations, not only in load case 2, is that modelling the steel with MAT_024+DIEM resulted in weaker heat affected zones, causing the spot welds to fail more readily. This could most likely be explained by the fact that incorrect material parameters has been used to model the heat affected zones. Figure 8.2 depicts a region where the spot-welds has failed in the DIEM model, but not in CrachFEM.

9 A study on the influence of kinematic hardening

9.1 Introduction

The existence of path independent variable spaces relies on the assumption that isotropic hardening holds [2]. In cases of non-linear and broken strain paths the hardening is never purely isotropic. Hence, it is of interest to find out how large of an error this assumption generates, and if these errors are small enough to be acceptable from an engineering point-of-view.

As an alternative to the conventional analytical M-K approach discussed in Section 4.3, an FE-based approach is sometimes adopted. Instead of introducing an imperfection band a shell mesh with randomly varying thicknesses is used. In this case a 10x10 mm boron steel sheet discretized with 100x100 plane stress quad elements. The boundaries of the sheet were subjected to prescribed displacements such that linear strain paths within the mesh were obtained. The prescribed boundary displacements were incrementally increased until a strain localization took place in the mesh, and a neck was formed.

The FE-based M-K approach is, as the name suggest, based on the same idea as the analytical M-K approach. The global strains at the time of incipient necking do provide a point on the FLC. In order to define the limit strain, the strain rate in the most strained element is compared to the global strain rate. When this ratio exceeds the predefined value k incipient necking is assumed. In accordance with [2] $k = 4$ was chosen in the current work. This can be expressed as

$$\frac{\dot{\epsilon}_{1,\,\mathrm{max}}}{\dot{\epsilon}_{1,\,\mathrm{glob}}} \geq k \tag{9.1}$$

The random thickness of the i:th shell element is defined by

$$t_i = t_0[1 + (2r - 1)d], \quad r \in [0, 1] \tag{9.2}$$

where t_0 is the nominal sheet thickness, r is a random parameter and d is an imperfection factor. An example of a localized neck in pre-strain case 2, $\rho_2 = 0.6$ is shown in Figure 9.1.

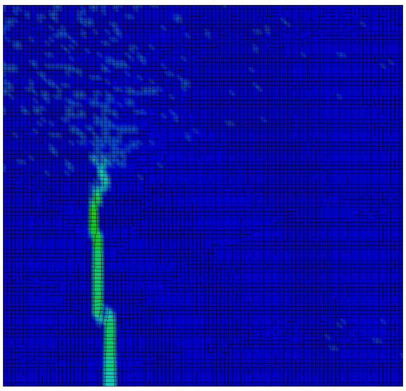

Figure 9.1: *The first principal strain rate fringe plotted as a neck develops in the FE-based M-K model in pre-strain case 2,* $\rho_2 = 0.6$.

By adopting this random sheet thickness distribution one comes around the problem of having to test different angles of the imperfection band, the randomness of the mesh resolves that issue.

9.2 The FE-based M-K method with linear strain paths assuming isotropic hardening

The magnitude of the imperfection factor d has been shown to be dependent on the strain path ρ [2]. In order to determine d an iterative process was adopted, in which simulations with various linear strain paths were performed. For each of these simulations an optimal value of the parameter d was determined so that the limit strains gave good conformity to the FLC. The optimal values of d, for different linear strain paths ρ, is plotted in Figure 9.2.

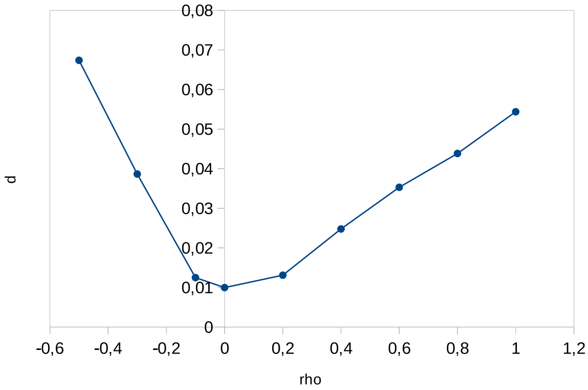

Figure 9.2: *Values of the thickness imperfection d giving good conformity to the experimental FLC.*

Figure 9.2 shows the optimal values of the parameter d for nine different linear strain paths $\rho \in [-0.5, 1]$. The imperfection factor corresponding to the linear strain paths in between these values were linearly interpolated. The FLC obtained with the FE-based M-K method is plotted in Figure 9.3a. By using the global average stresses and plastic strains at the onset of localized necking, the same limit curve was plotted in the $\alpha - \bar{\epsilon}^p$ space in Figure 9.3b.

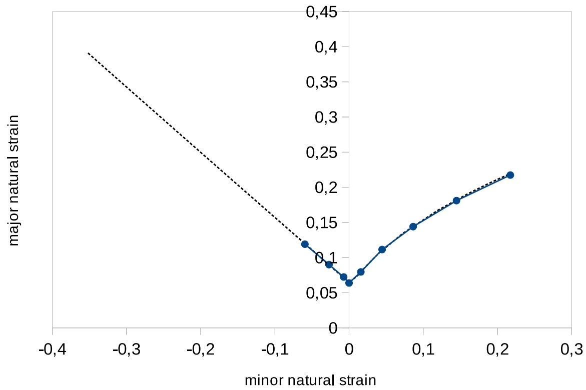

(a) *The limit curve and FLC in strain space.*

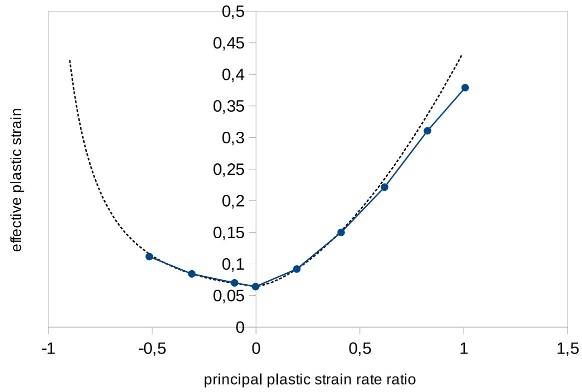

(b) *The limit curve and FLC in $\alpha - \bar{\epsilon}^p$ space.*

Figure 9.3: *The limit curve obtained when applying linear strain paths to the FE-based M-K model.*

Figure 9.3b reveals that the obtained limit curve conforms to the FLC satisfactory in the $\alpha - \bar{\epsilon}^p$ space as well.

9.3 The FE-based M-K method with linear strain paths assuming mixed hardening

The material model used in these simulations was *MAT_225 (*MAT_VISCOPLASTIC_MIXED_HARDENING). This model is based on the elasto-plastic material model *MAT_024, but has the ability to cope with mixed hardening. The degree of kinematic hardening is controlled by the hardening parameter β. A value of the hardening parameter in the order of 0.7 is characteristic for many metals. This was assumed to be a sensible value for the studied boron steel as well.

Having read the work done by the authors of [9] the assumption was that β would not affect the limit curve prediction in the case of linear strain paths. This was investigated for $\beta = [0, 0.3, 0.5, 0.7, 1]$, where the sheet was subjected to linear strain paths in the range $\rho \in [-0.5, 1]$. The obtained limit curves are displayed in Figure 9.4.

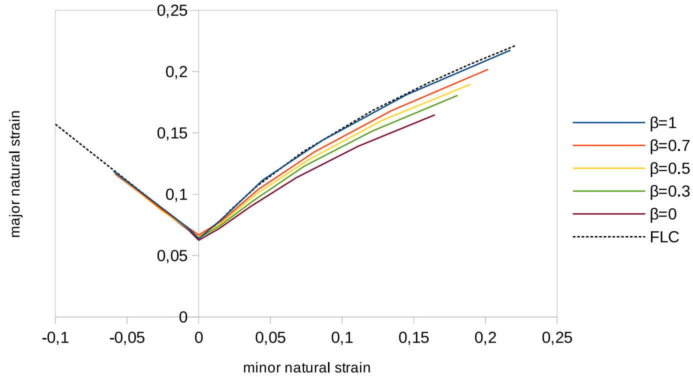

Figure 9.4: *Limit strains, in the case of linear strain paths, indicated by the FE-based M-K approach with five different values of the hardening parameter $\beta \in [0, 1]$. The black dashed line is the FLC.*

The initial hypothesis was that β would not affect the limit curve prediction in case of linear strain paths. However, Figure 9.4 suggests otherwise. This phenomenon can be explained by the size and location of the yield surfaces at onset of localized necking. The yield surfaces are plotted together with the stress paths inside and outside the neck for different values of β, in the linear equi-biaxial strain path case.

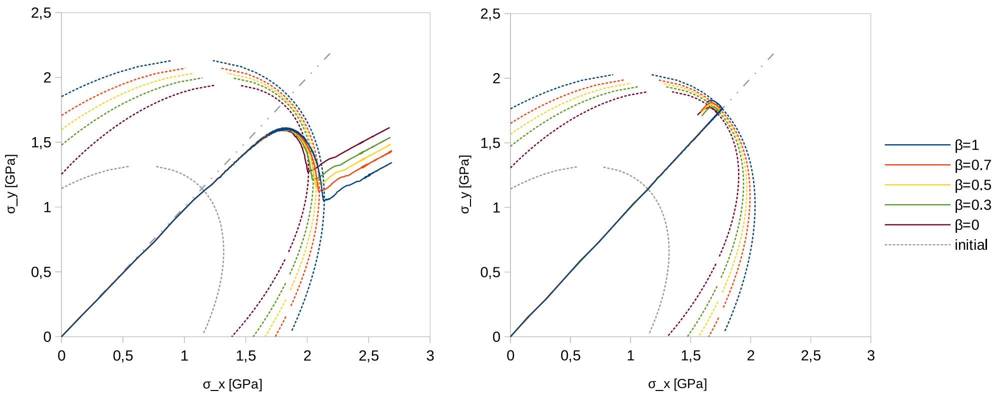

(a) *The yield surfaces inside the neck.*

(b) *The yield surfaces outside the neck.*

Figure 9.5: *The yield surfaces at onset of necking inside and outside the neck for different value of β, together with the corresponding stress paths. The grey dashed curve is the initial yield surface.*

Even though a global linear strain path was applied it did not result in a linear strain path in the elements where the neck was initialized, since those elements were approaching a state of plane strain, defecting the strain path from being linear. The difference in size and location of the yield surfaces in Figure 9.5a, caused by β, resulted in differences in stresses at onset of localized necking, i.e. the point in stress space corresponding to plane strain. This in turn led to the disparities in limit curve predictions observed in Figure 9.4.

9.4 The FE-based M-K method with biaxial strain paths assuming mixed hardening

In order to further investigate what effect an assumption of mixed hardening has on the limit strain prediction, biaxial strain paths were applied to the FE-based M-K model. The study was conducted for $\beta = [0.5\,, 0.7\,, 1]$, choosing one value on either side of the assumed correct value made it possible to detect trends in the predicted limit curves. The same strain paths as used in the single-element simulations in Section 6.1 were applied. In accordance with [2] the choice of the parameter d was based on the second part of the broken strain path.

When ρ changed sign an unstable behavior of the instability indicator could be observed. This phenomenon can be interpreted as a pseudo localization, and has been observed in physical experiments by Leotoing et al. [10]. In pre-strain case 3, and in particular for $\rho_2 = 1$, this pseudo localization caused the instability indicator to increase beyond $k = 4$. However, it was later re-stabilized at a value below $k = 4$, continuing until failure was indicated at a later stage, as demonstrated in Figure 9.6a. The same phenomenon occurred in pre-strain case 4, as can be seen in Figure 9.6b, but the instability indicator was not able to re-stabilize after ρ switched sign. Hence, in this particular case an instantaneous failure occurred.

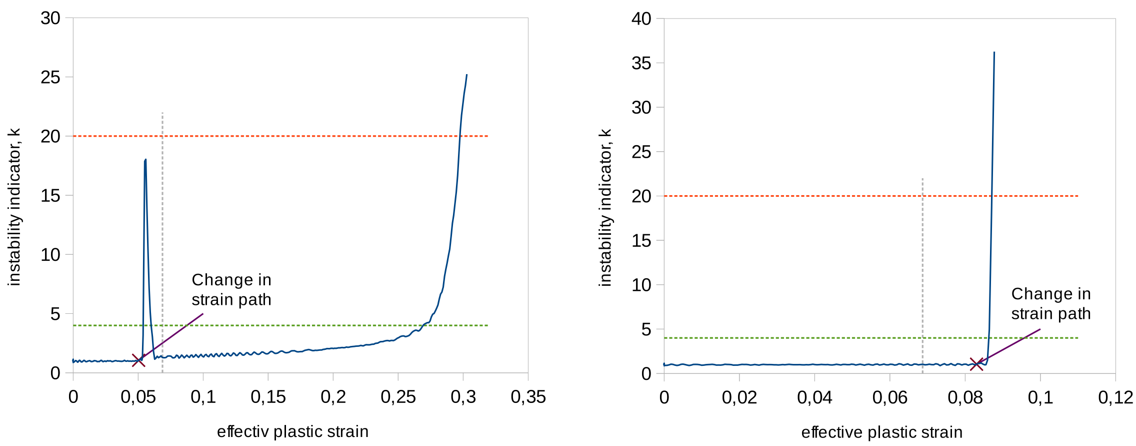

(a) *Pre-strain case 3 with* $\rho_2 = 1$

(b) *Pre-strain case 4 with* $\rho_2 = 1$

Figure 9.6: *The instability indicator vs. the effective plastic strain. The vertical gray line is the effective plastic strain at onset of necking in plane strain, and the cross marks the point where the direction of the strain path changed.*

In order to avoid getting indication of incipient necking from a pseudo localization, a second criterion was added saying that the instability indicator had to keep increasing beyond an upper limit of k = 20. This limit is plotted in Figure 28 along with the limit for incipient necking at k=4.

Limit curves from this investigation, presented in the principal strain space and the $\alpha - \bar{\epsilon}^p$ space, are shown in Figures 9.7-9.10.

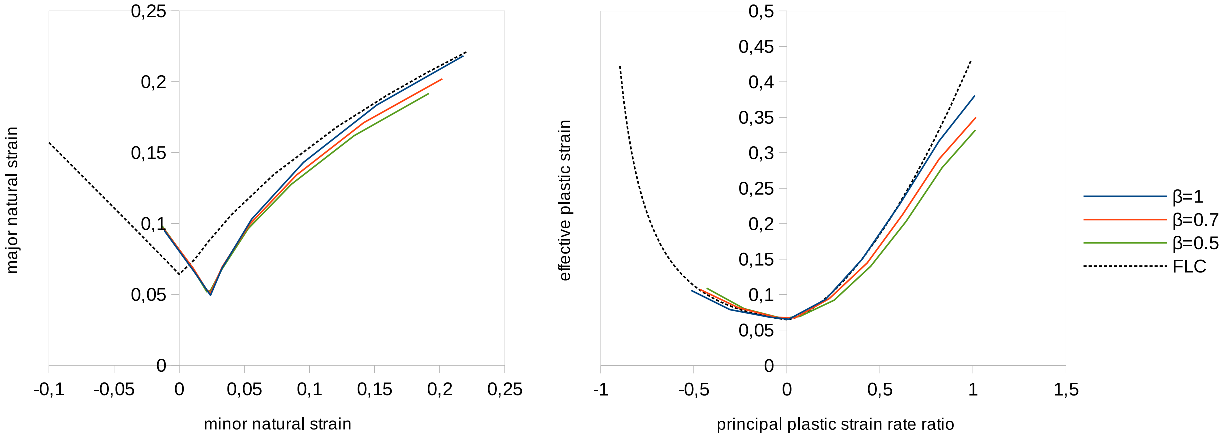

(a) *The principal strain space* (b) *The $\alpha - \bar{\epsilon}^p$ space*

Figure 9.7: *Limit curves indicated by the FE-based M-K approach in pre-strain case 1.*

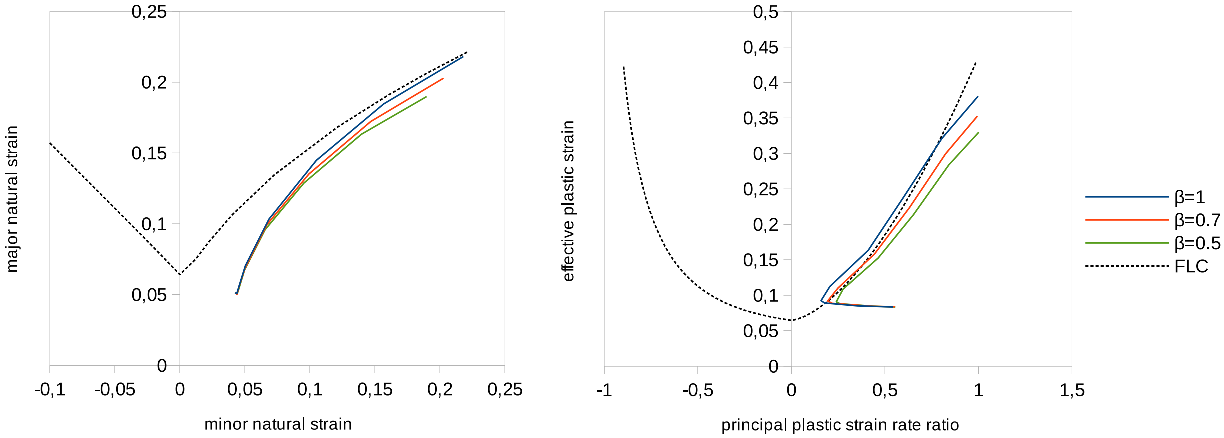

(a) *The principal strain space* (b) *The $\alpha - \bar{\epsilon}^p$ space*

Figure 9.8: *Limit curves indicated by the FE-based M-K approach in pre-strain case 2.*

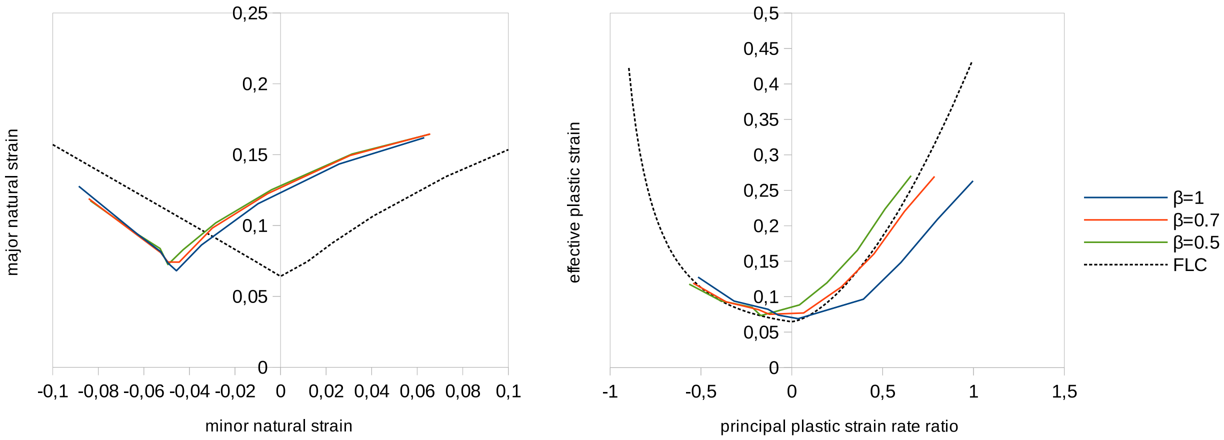

(a) *The principal strain space*

(b) *The* $\alpha - \bar{\epsilon}^p$ *space*

Figure 9.9: *Limit curves indicated by the FE-based M-K approach in pre-strain case 3.*

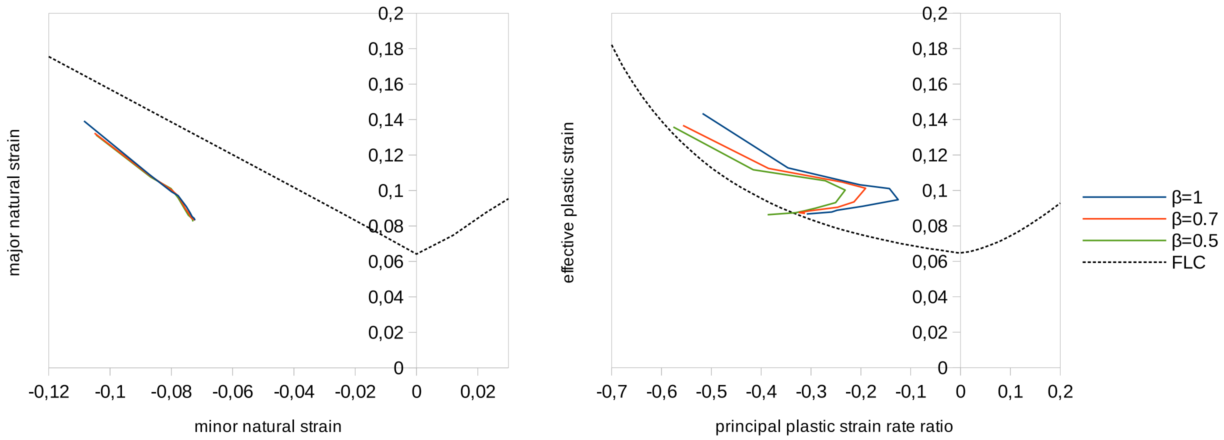

(a) *The principal strain space*

(b) *The* $\alpha - \bar{\epsilon}^p$ *space*

Figure 9.10: *Limit curves indicated by the FE-based M-K approach in pre-strain case 4.*

9.5 Observations and discussion

There are differences in the predicted limit curves for different values of β, i.e. kinematic hardening does affect the limit curve prediction. An observation is that β seems to affect the left part of the limit curves to a lesser extent than in the right part. This can again be explained by the evolution of the yield surfaces. For strain paths corresponding to the left part of the limit curves the yield surfaces expanded and translated in such a way that the points in stress space corresponding to plane strain coincided more closely for different values of β.

The limit curves obtained with the FE-based M-K model, resulting from a positive pre-strain, conform rather well to the FLC in the $\alpha - \bar{\epsilon}^p$ space. This is in agreement with the results obtained from DIEM and VCC in the single element simulations. However, when a negative pre-strain was applied the predicted limit curves did not conform as well, and β seems to have a greater influence in these cases. Furthermore, the M-K method indicated, just like the VCC-model, direct failure at certain changes in strain paths when the pre-strain was above the effective plastic strain corresponding to incipient necking in plane strain. Experiments performed by Leotoing et al. [10], where this phenomena was captured, further strengthens the obtained results.

10 Concluding remarks and future work

The FE-based M-K model and recent physical experiments performed by Leotoing et al. [10] both indicate that the instantaneous failure phenomenon do occur in reality. This fact speaks in the VCC-model's favor. However, no experiments, to the current authors knowledge, has been performed applying continuous broken strain paths to boron steel sheets. This is suggested in the future to confirm that the instantaneous failure is exhibited by boron steel as well.

The single element simulations revealed no differences between DIEM and the VCC-model. However, in the crash box simulations obvious differences emerged. It was concluded that the differences was entirely caused by the way the models predict failure. Work was put down to find the reason for this behaviour. The Lobatto integration scheme was adopted, but it was found that the disparities remained. To find the answer it is assumed that investigation of the the material model source codes would be helpful.

The results obtained from the crash box simulations are different when comparing the models. However, since no physical tests have been executed it is impossible to say what model yields the correct results. Hence, experimental validation of these simulations would be beneficial.

There were difficulties with making the VCC-model work together with CrachFEM at Volvo Cars. Due to this the VCC-model was not run in the full scale car simulations. To get a more realistic vehicle model material cards has to be prepared for all steel grades, i.e. the materials in CrachFEM has to be translated to be compatible with the VCC-model. Resolving these issues is something that is suggested to be done in the future.

The FE-based M-K model indicated that kinematic hardening does have an effect on the limit curve prediction. For the most part, the limit strains are rather similar independently of the hardening parameter β. This strengthens the assumption that failure curves in the VCC-model can be statically expressed in the $\alpha - \bar{\epsilon}^p$ space. However, in pre-strain case 3 the hardening parameter seems to have a larger influence on the limit curves in the $\alpha - \bar{\epsilon}^p$ space. From an engineering point-of-view the influence of kinematic hardening is not deemed large enough to claim that the assumption of isotropic hardening in the VCC-model is not valid.

Some of the findings in the current work indicate that the VCC-model certainly have potential of being a suitable alternative to CrachFEM. However, other results obtained makes it difficult to fully answer the question that was the main objective of this work. To do this further work has to be put down, where experimental validation of the simulations is considered the most important. What could be said with certainty is that, compared to CrachFEM, the VCC-model seem to be a conservative model.

References

[1] Transportstyrelsen. *Olycksstatistik - 23 personer omkom på vägarna i december.* 2015. URL: http://www.transportstyrelsen.se/sv/vagtrafik/statistik-och-register/Vag/Olycksstatistik/ (visited on 01/08/2016).

[2] K. Mattiasson, J. Jergéus, and P. DuBois. On the prediction of failure in metal sheets with special reference to strain path dependence. *International Journal of Mechanical Sciences* **88** (2014), 175–191. ISSN: 0020-7403. DOI: http://dx.doi.org/10.1016/j.ijmecsci.2014.08.006. URL: http://www.sciencedirect.com/science/article/pii/S0020740314002719.

[3] M. Costas, J. Díaz, L. Romera, S. Hernández, and A. Tielas. Static and dynamic axial crushing analysis of car frontal impact hybrid absorbers. *International Journal of Impact Engineering* **62** (2013), 166–181. ISSN: 0734-743X. DOI: http://dx.doi.org/10.1016/j.ijimpeng.2013.06.011. URL: http://www.sciencedirect.com/science/article/pii/S0734743X13001371.

[4] A. Sandahl. *Crash CAE in the all new Volvo XC 90 & SPA Platform.* Volvo Cars, Safety Centre. 2014. URL: https://www.dynamore.se/en/resources/papers/2014-nordic-ls-dyna-forum-2013-presentations/crash-cae-in-the-all-new-volvo-xc90.

[5] K. Runesson, P. Steinmann, M. Ekh, and A. Menzel. *Constituitive Modeling of Engineering Materials - Theory and Computation.* Vol. I. General Concepts of Inelasticity. Department of Applied Mechanics, Chalmers University of Technology, 2015.

[6] T. B. Stoughton and J. W. Yoon. A new approach for failure criterion for sheet metals. *International Journal of Plasticity* **27**.3 (2011), 440–459. ISSN: 0749-6419. DOI: http://dx.doi.org/10.1016/j.ijplas.2010.07.004. URL: http://www.sciencedirect.com/science/article/pii/S0749641910000951.

[7] H. Aretz. A less hypothetical perspective on rate-independent continuum theory of metal plasticity. *Mechanics Research Communications* **33**.5 (2006), 734–738. ISSN: 0093-6413. DOI: http://dx.doi.org/10.1016/j.mechrescom.2006.01.006. URL: http://www.sciencedirect.com/science/article/pii/S0093641306000152.

[8] *MF GenYld+CrachFEM 4.2 User's Manual. Theory.* Version 4.2. MATFEM, 2014.

[9] J. He, D. Zeng, X. Zhu, Z. C. Xia, and S. Li. Effect of nonlinear strain paths on forming limits under isotropic and anisotropic hardening. *International Journal of Solids and Structures* **51**.2 (2014), 402–415. ISSN: 0020-7683. DOI: http://dx.doi.org/10.1016/j.ijsolstr.2013.10.013. URL: http://www.sciencedirect.com/science/article/pii/S0020768313004022.

[10] L. Leotoing and D. Guines. Investigations of the effect of strain path changes on forming limit curves using an in-plane biaxial tensile test. *International Journal of Mechanical Sciences* **99** (2015), 21–28. ISSN: 0020-7403. DOI: http://dx.doi.org/10.1016/j.ijmecsci.2015.05.007. URL: http://www.sciencedirect.com/science/article/pii/S0020740315001861.

[11] *LS-DYNA keyword user's manual. Volume I.* Version R8.0. Livermore Software Technology Corporation (LSTC), 2015. URL: http://www.dynasupport.com/manuals/ls-dyna-manuals/ls-dyna-manual-r-8.0-vol-i.

[12] *LS-DYNA keyword user's manual. Volume II, Material Models.* Version R8.0. Livermore Software Technology Corporation (LSTC), 2015. URL: http://www.dynasupport.com/manuals/ls-dyna-manuals/ls-dyna-manual-r-8.0-vol-ii.